Materials Advances

ROYAL SOCIETY OF CHEMISTRY

PAPER

View Article Online
View Journal

Check for updates

Cite this: DOI: 10.1039/d6ma00075d

# Tailoring the properties of (TiZrHfV)$B_2$ high-entropy diborides *via* elemental concentration tuning: a first-principles approach

Nabila Tabassum and Yamini Sudha Sistla *

Received 17th January 2026,
Accepted 24th March 2026

DOI: 10.1039/d6ma00075d

rsc.li/materials-advances

High entropy diboride (HEB) ceramics are prospective materials for thermal protection systems and high temperature structural materials due to their excellent heat resistance, high temperature stability, super hardness, and wear resistance. The efficacy of high entropy ceramics lies in their tailorable properties and compositional flexibility. The present study uses first principles methods to design tailor made Ti, Zr, Hf, and V based HEBs with enhanced structural, mechanical, and thermal stability by tuning the stoichiometry of constituent metals. The thermodynamic phase and structural stability of 18 HEB compositions with varied elemental stoichiometry was confirmed using $\Delta H_{mix}$, $\Delta G_{mix}$, and enthalpy–entropy parameters and band-filling theory. A Vickers hardness of 35.72–43.22 GPa suggests the super-hardness of studied HEBs. Higher fractions of Ti in HEBs ($Ti_{0.42}Zr_{0.17}Hf_{0.25}V_{0.17}B_2$ and $Ti_{0.42}Zr_{0.25}Hf_{0.25}V_{0.08}B_2$) favored enhanced hardness while Hf rich $Ti_{0.08}Zr_{0.25}Hf_{0.42}V_{0.25}B_2$ showed the highest fracture toughness of 3.65 MPa $m^{1/2}$. Almost all non-equiatomic compositions displayed higher melting points (3480–3934 K) and $Ti_{0.33}Zr_{0.25}Hf_{0.25}V_{0.17}B_2$ exhibited the highest melting point of 3934 K. The highest Young's (539 GPa), shear (238 GPa), and bulk (246 GPa) moduli exhibited by the HEB having the highest Ti and lowest V concentrations ($Ti_{0.42}Zr_{0.25}Hf_{0.25}V_{0.08}B_2$) indicate remarkable elastic rigidity and superior resistance to shape and volume deformation. The findings accentuate the compositional flexibility of HEBs and highlight the importance of stoichiometry tailoring to develop HEBs with enhanced mechanical, thermodynamic, and structural stability. The present study emphasizes the effectiveness and superior properties of non-equiatomic compositions compared to the widely explored equiatomic compositions.

## 1. Introduction

Ceramic materials, due to their ultra-high melting points (>3000 °C), remarkable hardness, corrosion and wear resistance, better thermal insulation, and lightweight properties, are always preferred over metallic alloys in several applications such as furnaces and high temperature engine components, especially when resistance to extreme heat and corrosion is preferred.[1] High entropy ceramics (HECs) are solid solutions characterized by high configurational entropy due to the presence of four or more metallic cations or non-metallic anions in equal or unequal atomic fractions. Since their inception a decade back, HECs have been of great interest to researchers 0due to their unique, tailorable, and superior properties.[2,3] The HECs are interesting materials as they exhibit enhanced properties compared to the average of the constituent single metal ceramics. Most of the available literature focused on multi-cation (metal)- plus single anion (non-metal)-type HECs. The single anion type HECs based on oxides, borides, carbides, nitrides, sulfides, and silicides were widely reported in the literature.[1–6] The HECs, consisting of refractory elements, typically exhibit enhanced thermal stability and wear resistance.[4] HECs displaying super hardness (≥40 GPa) are a new class of materials that have attracted major attention due to their wide range of applications in wear and corrosion-resistant coatings, cutting tools, abrasives, and high-temperature applications.[1,2,5] The effect of composition and the atomic fractions of individual metals on improving the mechanical properties, lowering thermal conductivity, and improving hardness and fracture toughness of high entropy materials is widely discussed in the literature.[6]

High entropy transition metal diborides (mentioned as HEBs hereafter) are reported to exhibit remarkable mechanical properties such as high hardness, strength, melting points, oxidation resistance, and low thermal conductivity, which make them suitable for high-temperature applications (>2000 °C) compared to transition metal carbides and nitrides.[7,8] Their exceptional properties typically result from the strong interatomic interactions, compositional complexity, and configurational

---

Department of Chemical Engineering, Shiv Nadar Institution of Eminence Deemed to be University, Gautam Buddha Nagar, Uttar Pradesh 201314, India. E-mail: yamini.sistla@snu.edu.in

disorder as the constituent atoms occupy random lattice sites, which results in lattice distortion.[9–11] High entropy diborides (HEBs) consisting of metals such as Hf, Ta, Zr, Nb, Mo, and Ti have caught the attention of various researchers.[8,9] Liu *et al.* have reported the mechanical and thermal properties of an equiatomic $(Ti_{0.2}Zr_{0.2}Nb_{0.2}Hf_{0.2}Ta_{0.2})B_2$ HEB. They reported that the HEB exhibited a fracture toughness of 4.2 MPa $m^{1/2}$, Vickers hardness of 17.7 GPa, and low thermal conductivity at room temperature.[8] Storr *et al.* reported that the HEBs $(HfZrTiTaMo)B_2$ and $(HfZrNbTaMo)B_2$ showed Vickers hardness values of 38 GPa and 24.4 GPa, respectively, making them super hard materials.[12] Gild *et al.* have experimentally studied seven equiatomic HEBs such as $(Hf_{0.2}Zr_{0.2}Ta_{0.2}Nb_{0.2}Ti_{0.2})B_2$, $(Hf_{0.2}Zr_{0.2}Ta_{0.2}Mo_{0.2}Ti_{0.2})B_2$, $(Hf_{0.2}Zr_{0.2}Mo_{0.2}Nb_{0.2}Ti_{0.2})B_2$, $(Hf_{0.2}Mo_{0.2}Ta_{0.2}Nb_{0.2}Ti_{0.2})B_2$, $(Mo_{0.2}Zr_{0.2}Ta_{0.2}Nb_{0.2}Ti_{0.2})B_2$, $(Hf_{0.2}Zr_{0.2}W_{0.2}Mo_{0.2}Ti_{0.2})B_2$, and $(Hf_{0.2}Zr_{0.2}Ta_{0.2}Cr_{0.2}Ti_{0.2})B_2$.[13] They reported that the studied HEBs showed better oxidation resistance and hardness compared to the constituent single metal diborides.

Although various researchers provided theoretical predictions for high entropy ceramics and their experimental validation, the research was predominantly limited to equiatomic compositions. The experimental or theoretical studies on non-equiatomic high entropy ceramics are very limited in the open literature. With respect to high entropy diborides, even though HEBs display outstanding properties, the underlying fundamentals behind their exceptional properties are not fully understood. Therefore, the present study focuses on Ti, V, Zr, and Hf based high entropy diborides. To the best of our knowledge, only a single experimental research study is available in the literature on this particular HEB combination, which is also of equiatomic type.[14] Feltrin *et al.* have experimentally synthesized equiatomic $(Ti_{0.25}V_{0.25}Zr_{0.25}Hf_{0.25})B_2$ and reported a hardness of 33.2 GPa, Young's modulus of 466 GPa, and fracture toughness of 4.1 MPa $m^{1/2}$.[14] No literature is available on the non-equiatomic composition of this type of HEB consisting of Ti, V, Zr, and Hf. The constituent metal diborides $TiB_2$, $VB_2$, $HfB_2$ and $ZrB_2$ can be ranked in the following order with respect to some key properties: (i) melting point: $HfB_2 > ZrB_2 > TiB_2 > VB_2$, (ii) oxidation and corrosion resistance: $HfB_2 > ZrB_2 > TiB_2 > VB_2$, (iii) hardness: $HfB_2 > TiB_2 > ZrB_2 > VB_2$, and (iv) elastic modulus: $HfB_2 > TiB_2 > ZrB_2 > VB_2$. Considering the properties of pure metal diborides, it is interesting to investigate the effect of tuning the atomic fractions of these constituent elements on various properties of the resulting HEBs. This approach, in a way, optimizes the composition of Ti, V, Zr, and Hf based HEBs for more tailored properties. Establishing the fundamental rationale behind the observed macroscopic properties, such as the mechanical and thermal stability of HECs, based on the composition and concentration of individual elements, microstructure, phase stability, atomic-level disorder, lattice distortion, and cocktail effect, needs a thorough investigation.[15–17] In the exploratory stage, it will be highly resource-consuming and expensive to perform experimental investigation. Furthermore, experimental characterization techniques are not capable enough to elucidate the atomic-level complex interactions that govern the properties of materials. Therefore, first principles methods, such as density functional theory (DFT), play an instrumental role in establishing the atomic-level picture of compositional complexity, atomic disorder, lattice distortion, and their impact on mechanical, thermal, and chemical behavior. This accelerates the innovations in designing new HEC compositions by precisely evaluating the effect of the electronic structure on the physical, chemical, mechanical, and thermal properties. The novelty of the present study lies in reporting various non-equiatomic HEBs based on Ti, Zr, Hf, and V elements, which have superior mechanical and thermal properties compared to the equiatomic $(Ti_{0.25}V_{0.25}Zr_{0.25}Hf_{0.25})B_2$ while meeting the solid solution formation criteria.

## 2. Computational methodology

The crystal structures of the HEBs with varied atomic fractions of constituent metals were generated through the special quasi-random structure (SQS) protocol using ATAT as implemented in the pipeline pilot of BIOVIA Material Studio software version 2022. While generating the SQS, it was ensured that the crystal structure has a nearly cubic lattice ($a \approx b \approx c, \alpha \approx \beta \approx \gamma \approx 90^\circ$). To achieve this, the 7th nearest neighbor (NN) distance (7.54 Å) was used as a cutoff for the pair correlation, and the 3rd NN distance (5.17 Å) was used as a cutoff for the triplet correlation. The SQS structures of 18 HEB compositions comprising various atomic fractions of Ti, Hf, Zr, and V were generated and are presented in S1, SI. Each HEB comprised of 72 atoms, in which the number of boron atoms was fixed while the number of metal atoms (Ti, Hf, Zr, and V) was changed as per atomic fractions. The HEB structures were investigated for electronic, structural, mechanical, and thermal properties using plane wave DFT as implemented in the CASTEP module of BIOVIA Material Studio 2022 version. Generalized gradient approximation (GGA) with Perdew–Burke–Ernzerhof (PBE) exchange and correlation potential was chosen to handle the exchange–correlation potential. OTFG ultrasoft pseudopotentials were used to describe the nucleus–electron interaction. For geometry optimization, the Broyden–Fletcher–Goldfarb–Shanno (BFGS) algorithm was used to get a stable structure. For geometry optimization of the structure, the plane-wave cutoff energy was set at 440 eV. The Monkhorst–Pack (MP) method was employed to grid the first Brillouin zone with a 2 × 2 × 1 *k*-point mesh in reciprocal lattice space. During the full cell geometry optimization of SQS of HEBs, the total energy per atom was made sure to be less than $5.0 \times 10^{-6}$ eV per atom and 0.01 eV $Å^{-1}$ forces on a single atom, respectively. The SCF tolerance was set to $5.0 \times 10^{-7}$ eV per atom. Furthermore, the total stress tensor was reduced to the order of 0.02 GPa, with a maximum displacement of an atom to less than $5 \times 10^{-4}$ Å.

The elastic constants of the bulk crystal were calculated using the finite strain method. This approach expresses the stress–strain relationship in the standard Voigt notation of the generalized Hooke's law as $\sigma_i = \sum_j C_{ij}\varepsilon_j \ (i,j = 1-6)$, where $\sigma_i$ and $\varepsilon_j$ represent the stress and strain components, respectively, and $C_{ij}$ denotes the elements of the elastic stiffness matrix.[15,21] The crystal was subjected to both compressive and tensile strains in the range of −0.7% to +0.7%, with six equal increments (−0.007, −0.0042, −0.0014, +0.0014, +0.0042, and +0.007). This strain amplitude ensures that the deformation remains within the linear elastic regime while providing sufficient numerical accuracy for the determination of the elastic constants. The geometries of the six crystal structures after applying the deformations were optimized and resulting stresses were used to obtain the elastic constants from the Hooke's law. The cut-off energy for the geometry optimization steps required to compute the stiffness matrix calculation was set to 440 eV. Furthermore, the convergence threshold for the energy change was set to $1.0 \times 10^{-5}$ eV per atom, the maximum force was set to 0.03 eV Å$^{-1}$, and the maximum displacement of atoms was set to 0.001 Å$^{-1}$. The stiffness matrix (elastic constants) of all the SQS structures of the 18 HEB compositions was thus determined at $T$ = 0 K and $P$ = 0 GPa to study the mechanical properties. The Voigt–Reuss–Hill (VRH) approximation was used to calculate the elastic moduli, such as bulk modulus ($B$), shear modulus ($G$), Young's modulus ($E$), Poisson's ratio ($\nu$), hardness ($H_V$), and fracture toughness ($K_{IC}$), from the elastic constants or stiffness matrix ($C_{ij}$).

## 3. Results and discussion

### 3.1. Phase stability

The thermodynamic phase stability of the 18 HEB compositions was evaluated using various parameters such as enthalpy of mixing, entropy of mixing, Gibbs free energy of mixing, and enthalpy–entropy omega parameter as defined in eqn (1)–(4).[18]

$$\Delta H_{\text{mix}} = \left(H_{\text{total}} - \sum_{i=1}^{n} N_i H_i\right) \Big/ \sum_{i=1}^{n} N_i \tag{1}$$

where $N_i$ is the number of the $i$th metal diboride unit, $H_i$ is the enthalpy of individual metal diboride, and $H_{\text{Total}}$ is the enthalpy of the HEB.

The configurational entropy of mixing ($\Delta S_{\text{mix}}$) provides an estimate for the degree of randomness of the constituent metal diborides and signifies the entropy-driven phase stability for the formation of a single-phase solid solution. The $\Delta S_{\text{mix}}$ can be calculated as per eqn (2).[15,18]

$$\Delta S_{\text{mix}} = -R \sum_{i=1}^{n} x_i \ln x_i \tag{2}$$

where $x_i$ is the concentration of the $i$th metal diboride and $R$ is the universal gas constant.

The thermodynamic potential of phase stability of HEBs was evaluated from the Gibbs free energy of mixing ($\Delta G_{\text{mix}}$) as per eqn (3) below.[15,18]

$$\Delta G_{\text{mix}} = \Delta H_{\text{mix}} - T\Delta S_{\text{mix}} \tag{3}$$

where $T$ is the temperature. The higher $\Delta S_{\text{mix}}$ indicates that the higher degree of disorder in the atomic arrangement plays a critical role in the phase stability of solid solution and also overcomes any positive value of the enthalpy of mixing. The enthalpy of mixing should be in the range of −15 to +5 kJ mol$^{-1}$ for stable solid solutions of high entropy materials. Therefore, a higher degree of randomness ensures that the formation of intermetallic phases or phase separation is hampered.[19]

Another critical parameter that is used to assess the solid solution phase stability of high entropy materials is the omega ($\Omega$) parameter, which is a function of enthalpy of mixing, entropy of mixing and melting temperature as calculated using eqn (4).[15–21]

$$\Omega = \frac{T_{\text{m}} \Delta S_{\text{mix}}}{\Delta H_{\text{mix}}} \tag{4}$$

$$T_{\text{m}}\ (\text{K}) = 553\ \text{K} + (4.51\ \text{K GPa}^{-1})C_{11} \quad \pm 300\ \text{K} \tag{5}$$

Since the lattice parameters of pure diborides are $a = b \neq c$, lattice parameter mismatch ($\delta$) was calculated as per eqn (6a)–(6c)

$$\delta_{\text{a}} = \sqrt{\sum_{i=1}^{N} x_i \left[1 - \left(\frac{a_i}{\sum_{i=1}^{N} x_i a_i}\right)\right]^2} \tag{6a}$$

$$\delta_{\text{c}} = \sqrt{\sum_{i=1}^{N} x_i \left[1 - \left(\frac{c_i}{\sum_{i=1}^{N} x_i c_i}\right)\right]^2} \tag{6b}$$

$$\delta = \sqrt{\sum_{i=1}^{N} \frac{x_i}{2} \left[\left(1 - \frac{a_i}{\sum_{i=1}^{N} x_i a_i}\right)^2 + \left(1 - \frac{c_i}{\sum_{i=1}^{N} x_i c_i}\right)^2\right]} \tag{6c}$$

where $x_i$, $a_i$ and $c_i$ respectively are the concentration and lattice parameters $a$ and $c$ of the $i$th metal diboride $MB_2$.

Table 1 presents various compositions of the HEBs studied in the present work and their composition codes for ease of discussion. The parameters to be evaluated to assess the thermodynamic phase stability and solid solution formation ability of all the HEBs are also reported in Table 1. The data in Table 1 confirm that all the 18 HEBs satisfied the solid solution formation criteria (*i.e.* $\delta < 6\%$, $-15 \leq \Delta H_{\text{mix}} \leq 5$ kJ mol$^{-1}$, $\Omega > 1$, $\Delta S_{\text{mix}}$ = 12 to 17.5 J mol$^{-1}$ K$^{-1}$ and negative $\Delta G_{\text{mix}}$). The phase stability criteria parameters for the 18 HEBs are as follows: $\delta$ = 2.48% to 3.81%, $\Delta H_{\text{mix}}$ = −1.48 to −7.60 kJ mol$^{-1}$, $\Delta S_{\text{mix}}$ = 10.88 to 11.53 J mol$^{-1}$ K$^{-1}$, $\Delta G_{\text{mix}}$ (300 K) = −4.61 to −10.73 kJ mol$^{-1}$, and $\Omega$ = 5.36 to 25.18. The $\delta$ parameter being less than 4% signifies that the lattice parameters of the individual metal diborides do not vary significantly. This will ensure the stability of single-phase solid solution and uniform crystal structure. Higher $\delta$ parameter values resulting from higher mismatch in the pure metal diboride lattice parameters would lead to destabilization of single-phase solid solution, formation of multiple phases and segregated multiple phases,

Table 1 Solid solution formation criteria for Ti, Zr, Hf and V based high entropy diborides (HEBs)

| Code | HEC | $\Delta S_{\text{mix}}$ (J mol$^{-1}$ K$^{-1}$) | $\Delta H_{\text{mix}}$ (kJ mol$^{-1}$) | $\Delta G_{298\text{K}}$ (kJ mol$^{-1}$) | $\Omega$ | $\Delta E_{\text{form}}$ (eV) | $\delta_a$ (%) | $\delta_c$ (%) | $\delta$ (%) | $\Lambda$ | $\Delta\chi_{\text{Pauling}}$ | $\Delta\chi_{\text{Allen}}$ |
|---|---|---|---|---|---|---|---|---|---|---|---|---|
| HEB-1 | $Ti_{0.25}Zr_{0.25}Hf_{0.25}V_{0.25}B_2$ | 11.53 | −6.96 | −10.39 | 5.78 | −727.75 | 2.73 | 4.37 | 3.65 | 0.87 | 4.64 | 2.43 |
| HEB-2 | $Ti_{0.42}Zr_{0.25}Hf_{0.08}V_{0.25}B_2$ | 11.29 | −3.88 | −7.24 | 6.83 | −904.24 | 2.23 | 3.88 | 3.17 | 1.12 | 4.15 | 1.85 |
| HEB-3 | $Ti_{0.42}Zr_{0.25}Hf_{0.17}V_{0.17}B_2$ | 10.52 | −3.41 | −6.55 | 6.64 | −1111.6 | 2.30 | 4.14 | 3.35 | 0.94 | 4.63 | 2.24 |
| HEB-4 | $Ti_{0.42}Zr_{0.17}Hf_{0.25}V_{0.17}B_2$ | 11.29 | −4.50 | −7.87 | 8.87 | −619.42 | 2.48 | 4.51 | 3.64 | 0.85 | 4.71 | 2.43 |
| HEB-5 | $Ti_{0.42}Zr_{0.08}Hf_{0.25}V_{0.25}B_2$ | 10.52 | −5.68 | −8.81 | 9.29 | −412.09 | 2.83 | 4.58 | 3.81 | 0.73 | 4.35 | 2.42 |
| HEB-6 | $Ti_{0.42}Zr_{0.25}Hf_{0.25}V_{0.08}B_2$ | 11.29 | −1.97 | −5.34 | 5.36 | −903.09 | 2.77 | 4.37 | 3.66 | 0.84 | 4.08 | 1.97 |
| HEB-7 | $Ti_{0.42}Zr_{0.17}Hf_{0.17}V_{0.25}B_2$ | 11.29 | −4.45 | −7.82 | 12.02 | −897.20 | 2.65 | 4.31 | 3.57 | 0.89 | 4.66 | 2.38 |
| HEB-8 | $Ti_{0.08}Zr_{0.25}Hf_{0.42}V_{0.25}B_2$ | 10.52 | −1.48 | −4.61 | 11.49 | −879.99 | 2.66 | 4.16 | 3.49 | 0.86 | 4.73 | 2.73 |
| HEB-9 | $Ti_{0.08}Zr_{0.25}Hf_{0.25}V_{0.42}B_2$ | 10.52 | −7.60 | −10.73 | 25.18 | −871.22 | 2.45 | 3.91 | 3.26 | 0.99 | 5.08 | 2.73 |
| HEB-10 | $Ti_{0.08}Zr_{0.33}Hf_{0.33}V_{0.25}B_2$ | 10.52 | −4.40 | −7.54 | 7.91 | −874.70 | 2.69 | 4.22 | 3.54 | 0.84 | 5.00 | 2.80 |
| HEB-11 | $Ti_{0.08}Zr_{0.25}Hf_{0.33}V_{0.33}B_2$ | 11.29 | −6.09 | −9.45 | 17.95 | −841.92 | 2.56 | 4.04 | 3.38 | 0.99 | 5.29 | 2.97 |
| HEB-12 | $Ti_{0.08}Zr_{0.33}Hf_{0.25}V_{0.33}B_2$ | 11.29 | −3.44 | −6.80 | 14.04 | −841.32 | 2.56 | 4.07 | 3.40 | 0.98 | 5.23 | 2.80 |
| HEB-13 | $Ti_{0.17}Zr_{0.25}Hf_{0.33}V_{0.25}B_2$ | 10.88 | −3.49 | −6.73 | 10.97 | −652.83 | 2.75 | 4.36 | 3.65 | 0.82 | 4.73 | 2.60 |
| HEB-14 | $Ti_{0.17}Zr_{0.25}Hf_{0.25}V_{0.33}B_2$ | 10.88 | −4.66 | −7.91 | 21.13 | −767.53 | 2.63 | 4.21 | 3.51 | 0.88 | 4.86 | 2.58 |
| HEB-15 | $Ti_{0.17}Zr_{0.33}Hf_{0.25}V_{0.25}B_2$ | 10.69 | −2.84 | −6.02 | 12.22 | −772.84 | 2.68 | 4.26 | 2.52 | 1.68 | 4.66 | 2.43 |
| HEB-16 | $Ti_{0.33}Zr_{0.25}Hf_{0.17}V_{0.25}B_2$ | 10.69 | −2.10 | −5.28 | 9.38 | −986.33 | 2.61 | 4.22 | 2.48 | 1.74 | 4.45 | 2.20 |
| HEB-17 | $Ti_{0.33}Zr_{0.25}Hf_{0.25}V_{0.17}B_2$ | 10.69 | −4.69 | −7.87 | 7.30 | −976.46 | 2.78 | 4.43 | 2.61 | 1.57 | 4.39 | 2.23 |
| HEB-18 | $Ti_{0.33}Zr_{0.17}Hf_{0.25}V_{0.25}B_2$ | 10.88 | −5.89 | −9.13 | 9.75 | −547.84 | 2.78 | 4.48 | 2.64 | 1.56 | 4.54 | 2.42 |

and non-uniform crystal structures. Furthermore, the HEBs showed negative $\Delta H_{\text{mix}}$ which is within the limits of homogeneous solid solution formation, ensuring that the formation of the studied HEB compositions (with varied concentrations of Ti, Zr, Hf, and V) is thermodynamically favorable and the HEBs are energetically stable compared to the individual metal diborides. The lowest negative $\Delta H_{\text{mix}}$ indicates that the HEB structure is relatively stable compared to the constituent metal diborides, while the highest negative $\Delta H_{\text{mix}}$ indicates that the HEB is more stable compared to the constituent metal borides based on their concentrations. HEB-8 ($Ti_{0.08}Zr_{0.25}Hf_{0.42}V_{0.25}B_2$) showed the lowest $\Delta H_{\text{mix}}$ (−1.48 kJ mol$^{-1}$) and HEB-9 ($Ti_{0.08}Zr_{0.25}Hf_{0.25}V_{0.42}B_2$) showed the highest $\Delta H_{\text{mix}}$ (−7.60 kJ mol$^{-1}$). This indicates that at fixed concentrations of Ti and Zr, higher Hf concentration decreased the phase stability of the HEB, while higher concentration of V increased the phase stability. This trend could be attributed to the highest Pauling electronegativity of $VB_2$ (1.903) followed by $TiB_2$ (1.873), $ZrB_2$(1.803) and the lowest Pauling electronegativity of $HfB_2$ (1.793). Furthermore, the $\Delta S_{\text{mix}}$ of all the HEB compositions has satisfied the solid solution formation criteria. The $\Delta G_{\text{mix}}$ (at 300 K) confirms the thermodynamic feasibility of HEB formation at all temperatures. The $\Omega$ parameter infers how significant the entropy of mixing is over the enthalpy of mixing to stabilize the disordered solid solution. As per eqn (4), for $\Omega > 1$, the numerator of eqn (4) will be higher than the denominator indicating the dominance of configurational atomic randomness at the melting temperature of the material over the enthalpy of mixing, leading to the formation of a stable solid solution. On the other hand, for $\Omega < 1$, the denominator of eqn (4) will be higher than the numerator which indicates the dominance of the enthalpy of mixing over configurational randomness, leading to the formation of intermetallic phases due to strong interatomic interactions.[19] Table 1 confirms that the $\Omega$ parameter was greater than '1' for all the studied HEBs, ranging widely between 5.36 and 25.18, suggesting their thermodynamic stability and the favorability of solid solution formation. The $\Lambda$ parameter of HEBs as calculated using eqn (7) is presented in Table 1.

$$\Lambda = \frac{\Delta S_{\text{mix}}}{\delta^2} \tag{7}$$

The $\Lambda$ parameter demonstrates the stability of single-phase solid solutions by low $\delta$ (a measure of strain energy) and high $\Delta S_{\text{mix}}$. Formation of intermetallics is favored when $\Lambda$ is less than 0.24 while two-phase solid solution formation is favored for $0.24 < \Lambda < 0.96$, and single-phase solid solution is favored for $\Lambda > 0.96$.[19]

It can be seen from Table 1 that the $\Lambda$ parameter of most of the HEBs lie in the range of $0.24 < \Lambda > 0.96$ except for HEB-2 and HEB-15 to HEB-18. Therefore, except for HEB-2 and HEB-15 to HEB-18, the other HEB compositions show the possibility of forming two-phase solid solution crystal structures. The HEB-2, HEB-15, HEB-16, HEB-17 and HEB-18 have the potential of forming single phase solid solutions as their $\Lambda$ parameter is greater than 1 due to the dominating entropy factor as per eqn (7).

The classical Hume–Rothery rule states that a set of elements tend to form solid solution when the constituent elements have similar atomic sizes, valency, and electronegativity (Guo *et al.* 2011). The Pauling electronegativity difference ($\chi_{\text{Pauling}}$) and Allen electronegativity difference ($\chi_{\text{Allen}}$) parameters as determined from eqn (8a) and (8b), respectively, were used to evaluate the tendency of the studied HEBs to form single-phase solid solutions.[18,19]

$$\Delta\chi_{\text{Pauling}} = \sqrt{\sum_{i=1}^{n} C_i \left(\chi_i^{\text{Pauling}} - \sum_{j=1}^{n} C_j \chi_j^{\text{Pauling}}\right)^2} \tag{8a}$$

$$\Delta\chi_{\text{Allen}} = \sqrt{\sum_{i=1}^{n} C_i \left(1 - \frac{\chi_i^{\text{Allen}}}{\sum_{j=1}^{n} C_j \chi_j^{\text{Allen}}}\right)^2} \tag{8b}$$

where $\chi_i^{\text{Pauling}}$ and $\chi_j^{\text{Pauling}}$ are the Pauling electronegativities of $i$th and $j$th elements. $C_i$ is the concentration of $i$th element. Smaller electronegativity differences indicate that the atoms of the HEC can uniformly attract the electrons and therefore form stable solid solutions. On the other hand, a higher electronegativity difference favors the formation of amorphous phase. As reported by Li *et al.*, single phase solid solutions are favored when $\Delta\chi_{\text{Pauling}}$ values are less than 5.4% while the material tends to form multiple phases when $\Delta\chi_{\text{Pauling}} > 5.4\%$. Furthermore, Yurchenko *et al.* reported that the $\Delta\chi_{\text{Allen}}$ values greater than 7.0% along with an atomic size difference of greater than 5% favor the formation of laves phase (intermetallic compound).[20] The Pauling and Allen electronegativity mismatch values for the studied HEBs are mentioned in Table 1. The $\Delta\chi_{\text{Allen}}$ values were in the range of 1.87–2.97% and the $\Delta\chi_{\text{Pauling}}$ values were in the range of 4.08–5.29% for the HEB compositions studied. Therefore, according to the $\Delta\chi_{\text{Pauling}}$, all the HEBs tend to form single-phase solid solutions. As the $\Delta\chi_{\text{Allen}}$ was $<7\%$ for the studied HECs, and lattice parameter mismatch was less than 5%, the formation of laves phases (intermetallic compound) can be ruled out. Overall, the "$\Lambda$" parameter and electronegativity difference results collectively indicate that all the studied HEBs with un-equal concentrations of constituent metals have the tendency to form single phase solid solution.

### 3.2. Structural properties

The optimized stable energy structures of equiatomic HEB-1 ($Ti_{0.25}Zr_{0.25}Hf_{0.25}V_{0.25}B_2$) and of the other 17 HEB compositions are presented in S1, SI. Due to the presence of multiple metal atoms with different atomic sizes, the geometries of HEBs had stabilized as distorted cubic (triclinic) crystal structures. Though the distorted cubic structures usually show localized variations from perfect cubic symmetry, the local atomic arrangement in high entropy crystal structures produces regions that generally have similarity to cubic structures.[21,22] The lattice parameters, unit cell volume, and density of the optimized HEB crystal structures are shown in Fig. 1(a) and (b).

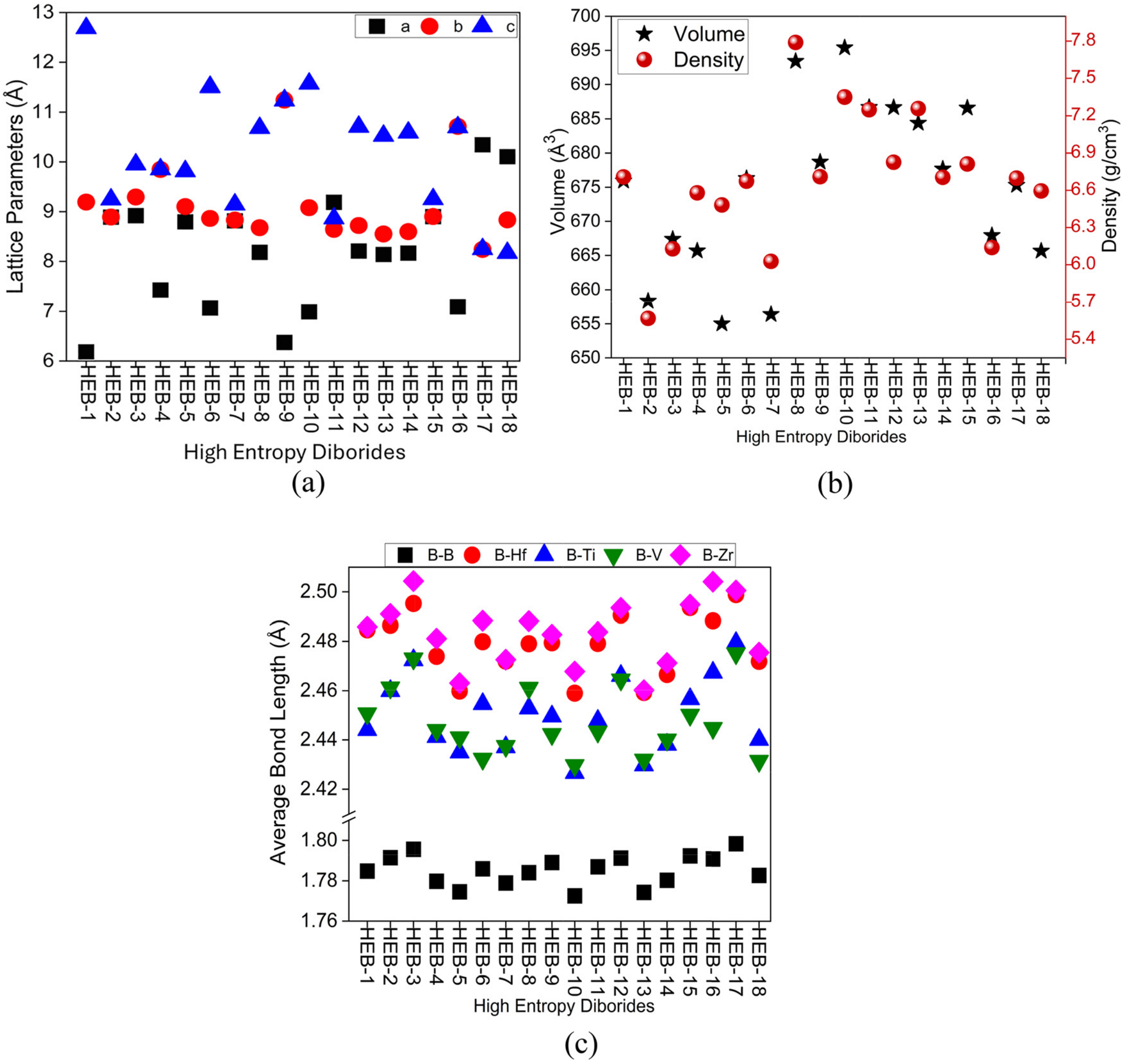

Fig. 1 Structural parameters of the Ti, Zr, Hf and V based HEBs: (a) lattice parameters, (b) unit cell volume and density, and (c) average bond length.

Fig. 1 comprehends that the lattice parameters, cell volume, and density vary significantly with the variation in the concentrations of Zr, Hf, Ti, and V in the investigated 18 HEB compositions. The lattice constant, a fundamental structural parameter of crystal structure, characterizes the changes in lattice position occupied by the constituent atoms resulting from the variations in the lattice stress. Furthermore, the lattice parameters, which indeed reflect the inter-atomic interactions, therefore directly influence the density of the material.[23] For the studied HEB compositions, the unit cell volume was in the range of 655 to 695 Å$^3$ while the density was in the range of 5.6 to 7.7 g cm$^{-3}$. The Hf rich composition HEB-8 ($Ti_{0.08}Zr_{0.25}Hf_{0.42}V_{0.25}B_2$) showed the highest cell volume (∼693 Å$^3$) and high density (∼7.78 g cm$^{-3}$). Furthermore, another Hf and Zr rich composition HEB-10 ($Ti_{0.08}Zr_{0.33}Hf_{0.33}V_{0.25}B_2$) also showed the highest cell volume (∼695 Å$^3$) and high density (∼7.35 g cm$^{-3}$).

The presence of higher concentration of lowest electronegative $HfB_2$ (1.793) and high atomic radius Hf (1.55 Å) in HEB-8 resulted in weak interatomic interactions (lowest $\Delta H_{mix}$ = −1.48 kJ mol$^{-1}$), leading to relatively large Hf—B bond lengths (Fig. 1(c)), loose lattice packing and higher lattice volume. Similarly, the presence of equal fractions (0.33) of low electronegative $HfB_2$ and $ZrB_2$ and high atomic radius Zr (1.6 Å) and Hf in HEB-10 resulted in $\Delta H_{mix}$ = −4.40 kJ mol$^{-1}$, leading to relatively large Hf—B and Zr—B bond lengths (Fig. 1(c)), loose lattice packing and higher lattice volume. Furthermore, the compositions having high atomic fractions of low molar mass elements Ti (47.86 g mol$^{-1}$) and V (50.94 g mol$^{-1}$) showed low density and the composition having a higher fraction of high molar mass elements Hf (178.49 g mol$^{-1}$) and Zr (91.22 g mol$^{-1}$) showed high density. Fig. 1(b) also confirms that the HEBs such as HEB-2, HEB-3, HEB-4, HEB-5, HEB-7, HEB-16, and HEB-18, which have Ti concentrations higher than the equiatomic concentration (*i.e.* 0.25) and equiatomic fraction of V (*i.e.* 0.25), showed relatively less unit cell volume and density compared to the equiatomic HEB ($Ti_{0.25}Zr_{0.25}Hf_{0.25}V_{0.25}B_2$). Low density is advantageous for advanced materials like high entropy materials, as they offer lighter yet stronger and efficient products in terms of properties and cost.

The average boron–boron (B–B) and metal–boron (M–B) bond lengths for each HEB composition are presented in Fig. 1(c), and only the M–B bond lengths are plotted in Fig. 1(d) for a more detailed view. It was observed that the bond lengths of Zr–B (∼2.5 Å) and Hf–B (∼2.48 Å) were relatively higher than those of Ti–B (2.45 Å) and V–B (2.42 Å) for all the HEBs studied. Considering the compositional complexity of the HEBs, making direct correlations between the M–B electronegativity difference and average bond lengths is not appropriate, because the average M–B bond length also depends on the M–M interactions as well. The ionic radii of Zr, Hf, Ti, and V are 1.60, 1.58, 1.46, and 1.35 Å, respectively. Therefore, the higher Zr–B and Hf–B bond lengths could be attributed to the larger atomic radii of Zr and Hf compared to Ti and V. Additionally, the B–B bond length was in the range of 1.77–1.79 Å for all the HEBs.

### 3.3. Mechanical properties

The elastic constants $C_{11}$, $C_{12}$, and $C_{44}$ of the 18 HEB compositions studied are presented in Fig. 2(a). Fig. 2(a) describes that for a particular HEB, the elastic constants followed the order of $C_{11} > C_{44} > C_{12}$. This is a common trend for any cubic crystal as the stress required for uniaxial (longitudinal) deformation is characteristically higher than the stress required for shear deformation, which in turn is higher than the stress required for volume changes. The $C_{11}$, $C_{12}$, and $C_{44}$ data, as reported in Fig. 2(a), confirm that all HEBs satisfy the Born–Huang mechanical stability criteria (as per eqn (9)), indicating that the materials are so stable that any small deformation needs energy input as the internal energy of the material increases with stress produced due to strain applied.

$$C_{11} > 0; \quad C_{44} > 0; \quad C_{11} - C_{12} > 0; \quad C_{11} + 2C_{12} > 0 \tag{9}$$

Born–Huang mechanical stability demands a positive elastic stiffness tensor so that the material is stable and does not show any unusual behavior.[24] For cubic crystals, the resistance of the material to shear deformations along their crystallographic planes can be understood using the Cauchy pressure ($C_{12}$–$C_{44}$). The Cauchy pressure (CP) directly involves the shear deformation constants associated with the (100) and (110) planes.[25] Positive CP ($C_{12}$–$C_{44} > 0$) indicates that the material is more resilient to shear deformation (related to $C_{12}$) than to isotropic compression or dilation (related to $C_{44}$) in the (100) plane, which is frequently linked to ductile materials or those that show plastic deformation in response to applied stress. A negative CP ($C_{12}$–$C_{44} < 0$) indicates that the material is more prone to shear deformation than to isotropic compression or dilation in the (110) plane. It is indicative of the material's brittleness in terms of ductility.[25] Based on the elastic constants, all the 18 HEBs showed negative Cauchy pressure ($C_{12}$–$C_{44} < 0$) as $C_{12}$ is less than $C_{44}$ (Fig. 2(a)). The negative Cauchy pressure indicates that the HEBs are brittle in nature due to the presence of interatomic directional covalent bonding existing between the metallic Ti, Zr, Hf, and V atoms and the non-metal B atom.

Due to the less flexibility of the directional covalent bonds, the HEBs could show brittle behavior under stress without any prior plastic deformation. The Voigt–Reuss–Hill (VRH) approximation was employed to calculate the polycrystalline elastic moduli, such as bulk modulus ($B$), shear modulus ($G$), Young's modulus ($E$), Poisson's ratio ($\nu$), fracture toughness ($K_{IC}$), hardness ($H_V$), and universal anisotropic index ($A^U$) as per eqn (10)–(24).[21–23]

$$B_V = (C_{11} + 2C_{12})/3 \tag{10}$$

$$B_R = \frac{1}{3S_{11} + 6S_{12}} \tag{11}$$

$$G_V = (C_{11} - C_{12} + 3C_{44})/5 \tag{12}$$

$$G_R = \frac{5}{4S_{11} - 4S_{12} + 3S_{44}} \tag{13}$$

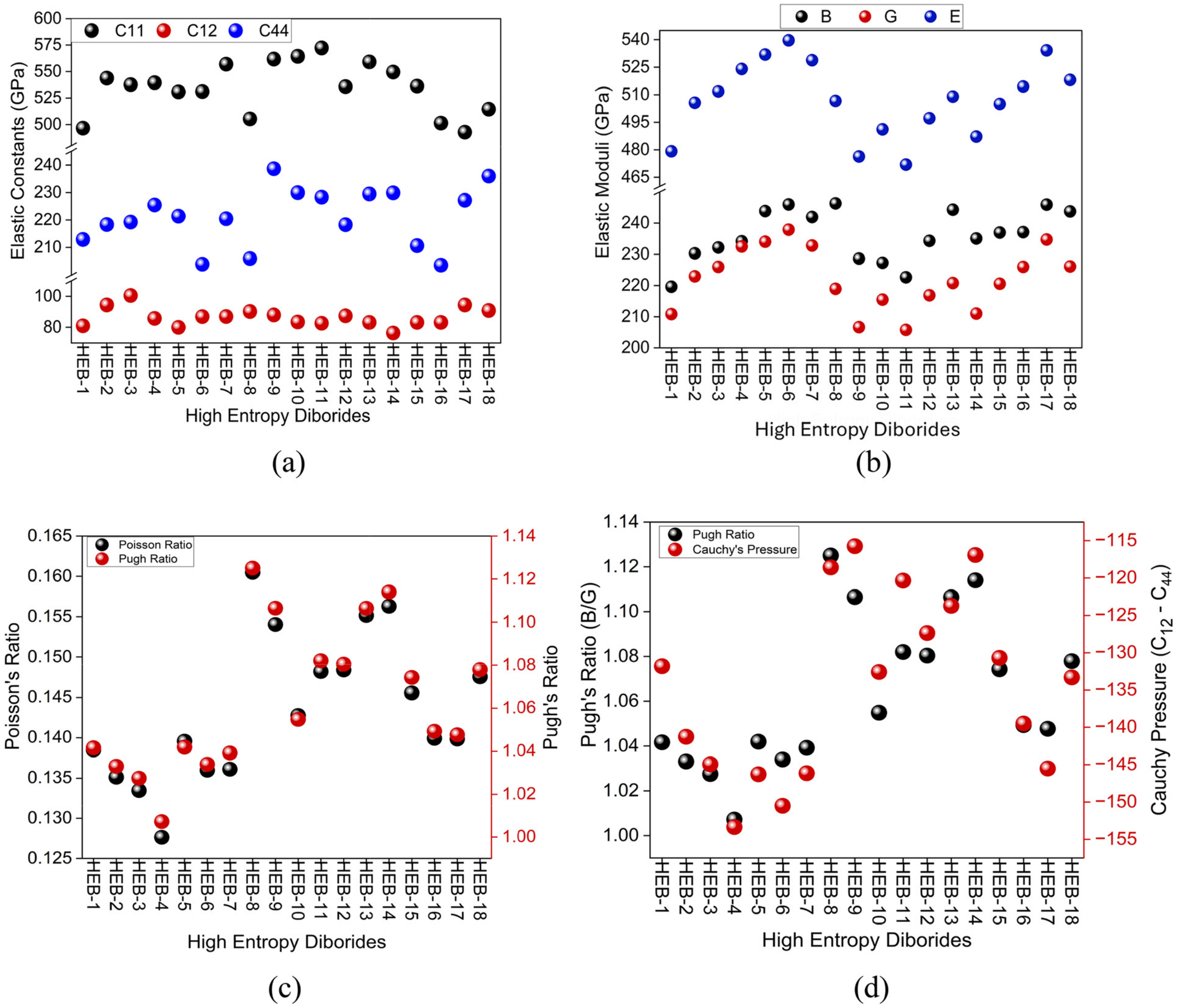

Fig. 2 Mechanical properties of TiZrHfV-based HEBs: (a) elastic constants, (b) elastic moduli, (c) Poisson's ratio *vs.* Pugh's ratio, and (d) Pugh's ratio *vs.* Cauchy pressure.

$$B = (B_R + B_V)/2 \tag{14}$$

$$G = (G_R + G_V)/2 \tag{15}$$

$$E = \frac{9BG}{3B + G} \tag{16}$$

$$\nu = \frac{3B - E}{6B} \tag{17}$$

$$\Theta_D = (h/k)[(3n/4\pi)(N_A\rho/M)]^{1/3}V_m \tag{18}$$

$$V_m = [(1/V_l^3 + 2/V_t^3)/3]^{-1/3} \tag{19}$$

$$V_t = (G/\rho)^{1/2} \tag{20}$$

$$V_l = [(3B + 4G)/3\rho]^{1/2} \tag{21}$$

Here, $C_{ij}$ refers to the stiffness matrix and $S_{ij}$ is the compliance matrix. $B$, $G$, and $E$ are elastic moduli ($B_V$ is the Voigt bulk modulus, $B_R$ is the Reuss bulk modulus, $G_V$ is the Voigt shear modulus, and $G_R$ is the Reuss shear modulus) and $\nu$ is Poisson's ratio for cubic crystals. $k$ is Boltzmann's constant, $h$ is Planck's constant, $N_A$ is Avogadro's number, $n$ is the number of atoms per cell, $\rho$ is the mass density of the crystal, $M$ is the molecular weight, $V_m$ is the average elastic acoustic wave velocity, $V_t$ is the transverse elastic acoustic wave velocity, and $V_l$ is the longitudinal acoustic wave velocity.

Another empirical indicator for differentiating between brittle and ductile materials is Pugh's ratio $B/G$. The material is deemed to be brittle when $B/G < 1.75$, while deemed to be ductile if $B/G \geq 1.75$.[11,25]

The universal anisotropy index ($A^U$), anisotropy in Young's modulus ($A^E$), anisotropy in linear compressibility ($\beta$) ($A^C$), and the anisotropy in shear modulus ($A^G$) were calculated by using the equations mentioned below.

$$A^U = \left(\frac{B_V}{B_R}\right) + 5\left(\frac{G_V}{G_R}\right) - 6 \tag{22}$$

$$A_E = E_{max}/E_{min}; \quad A_G = G_{max}/G_{min}; \quad A_C = \beta_{max}/\beta_{min}$$

where $E_{\max}$ and $E_{\min}$ are the maximum and minimum Young's moduli, $G_{\max}$ and $G_{\min}$ are the maximum and minimum shear moduli, and $\beta_{\max}$ and $\beta_{\min}$ are the maximum and minimum linear compressibilities.

Vickers hardness ($H_V$) as proposed by Tian *et al.*[26] and fracture toughness ($K_{IC}$) as proposed by Niu *et al.*[27] are calculated using the formulas below:

$$H_V = 0.92(G/B)^{1.137}G^{0.708} \tag{23}$$

$$K_{IC} = {V_0}^{1/6}G(B/G)^{1/2} \tag{24}$$

where $V_0$ is the volume per atom in m$^3$, $B$ is the bulk modulus, and $G$ is the shear modulus; $K_{IC}$ has the units of MPa m$^{0.5}$. Tian's model and Niu's model and the melting temperature from elastic constant $C_{11}$ (eqn (5)) provide good estimates of hardness, fracture toughness and melting temperature respectively of transition metal diborides. However, due to the structural complexity associated with the high entropy diborides, these models face certain limitations in providing good estimates of hardness and fracture toughness. One of the major limitations is that the models (crystal structures) of HEBs are developed by assuming ideal randomness in the arrangement of atoms in the lattice sites. However, in reality, the high entropy materials have high probability to exhibit local ordering. This can alter the inter-atomic bond strength compared to the ideal random arrangement. Furthermore, the empirical models assume that the HEBs form a homogeneous single-phase. However, in reality, there will be high probability of the formation of secondary phases based on synthesis procedures. This leads to differences in predicted values of hardness, fracture toughness and melting temperature from empirical models and actual experimental values. Nonetheless, these empirical models provide reasonably good estimates of the properties for comparison purposes.

The bulk modulus, shear modulus, and Young's modulus of all 18 HEBs are presented in Fig. 2(b). The bulk modulus of the HEBs, depending on the elemental concentration, was observed to be in the range of 219.61–246.30 GPa, while the shear modulus was in the range of 205.77–237.87 GPa, and the Young's modulus was in the range of 476.34–539.64 GPa. This wide range of elastic moduli reflect the strong influence of the concentration of constituent transition metals, interatomic interactions, and microstructure resulting from the lattice distortion due to high configurational entropy and the presence of multiple elements on the mechanical stability of the material. Among the HEB compositions studied, the Hf rich and Ti rich HEB-6 ($Ti_{0.42}Zr_{0.25}Hf_{0.25}V_{0.08}B_2$), HEB-8 ($Ti_{0.08}Zr_{0.25}Hf_{0.42}V_{0.25}B_2$), and HEB-17 ($Ti_{0.33}Zr_{0.25}Hf_{0.25}V_{0.17}B_2$) showed the highest bulk modulus, and the lowest bulk modulus was shown by the equiatomic composition HEB-1 ($Ti_{0.25}Zr_{0.25}Hf_{0.25}V_{0.25}B_2$). The higher bulk modulus signifies that the materials are incompressible and rigid and need higher pressures to cause any small volume changes, or the material is highly resistant to compression under pressure. Broadly, among the 18 HEBs, the compositions such as HEB-5, HEB-6, HEB-7, HEB-8, HEB-13, HEB-17, and HEB-18 would make harder materials, while the others are relatively softer (less resistant to volumetric changes under pressure). It was observed that the compositions having higher atomic fractions of Ti and Hf showed higher bulk modulus compared to other compositions. As per the literature, the diborides $HfB_2$ and $TiB_2$ exhibit a higher bulk modulus compared to $ZrB_2$ and $VB_2$.[28] This suggests that an increase in Hf and Ti concentrations could enhance the material's capability to resist volumetric compression under pressure.

Shear modulus, or the modulus of rigidity, is another critical property of materials that signifies the resistance of a material to shape deformation against applied shearing forces. Among the HEBs studied, the lowest shear modulus was shown by HEB-11 ($Ti_{0.08}Zr_{0.25}Hf_{0.33}V_{0.33}B_2$), HEB-9 ($Ti_{0.08}Zr_{0.25}Hf_{0.25}V_{0.42}B_2$), HEB-1 ($Ti_{0.25}Zr_{0.25}Hf_{0.25}V_{0.25}B_2$), and HEB-14 ($Ti_{0.17}Zr_{0.25}Hf_{0.25}V_{0.33}B_2$) in the increasing order (Fig. 2(b)). The HEBs such as HEB-6 ($Ti_{0.42}Zr_{0.25}Hf_{0.25}V_{0.08}B_2$), HEB-5 ($Ti_{0.42}Zr_{0.08}Hf_{0.25}V_{0.25}B_2$), HEB-17 ($Ti_{0.33}Zr_{0.25}Hf_{0.25}V_{0.17}B_2$), HEB-7 ($Ti_{0.42}Zr_{0.17}Hf_{0.17}V_{0.25}B_2$), and HEB-4 ($Ti_{0.42}Zr_{0.17}Hf_{0.25}V_{0.17}B_2$) showed the highest shear modulus in the decreasing order. Based on the observations, it can be inferred that a higher Ti concentration compared to other constituents has induced higher shear modulus, *i.e.*, resistance to brittle fracture, and therefore, the material can maintain its structural integrity. Furthermore, by keeping Zr concentration at 0.25, higher V concentrations compared to Ti and Hf have reduced the shear modulus. Due to the varied concentrations of constituent elements, the difference in atomic radii and bonding characteristics leads to increased atomic-level disorder. This alters the atomic packing and bond stiffness, which ultimately affects the material's resistance to deformation. Indeed, the first-principles studies have shown that electronic (bond populations) and lattice distortions induce elastic softening in HEBs as the disorder disrupts ideal atomic arrangements and weakens the bonding networks.[29] Furthermore, covalent bonding is crucial for the material's rigidity and high hardness. It is equally essential that the metal–boron (M–B) bonds avoid becoming excessively covalent. The crystal may exhibit structural irregularities and lattice distortions if the covalent nature of these bonds becomes excessively strong, which will disturb the material's resistance to compression and erode its overall structural integrity. On the other hand, when a metal is too ionic with boron (M–B), it will reduce the shear strength and the material is prone to brittleness.[30] Therefore, a balance of ionic and covalent bonds is desired for the material to exhibit the anticipated super hardness.

Among the HEB compositions studied, HEB-6 ($Ti_{0.42}Zr_{0.25}Hf_{0.25}V_{0.08}B_2$) and HEB-17 ($Ti_{0.33}Zr_{0.25}Hf_{0.25}V_{0.17}B_2$) showed the highest Young's modulus, while HEB-1 ($Ti_{0.25}Zr_{0.25}Hf_{0.25}V_{0.25}B_2$), HEB-9 ($Ti_{0.08}Zr_{0.25}Hf_{0.25}V_{0.42}B_2$), and HEB-11 ($Ti_{0.08}Zr_{0.25}Hf_{0.33}V_{0.33}B_2$) showed the lowest Young's modulus. The data indicate that for a fixed Zr concentration of 0.25, the compositions having higher atomic fractions of Ti and Hf and lower atomic fractions of V showed higher Young's modulus, while the compositions having low Ti and high V showed lower Young's modulus. The higher Young's modulus signifies higher stiffness of the material and its resistance to deformation, such as bending and stretching, under applied stress. On the other hand, a low Young's modulus indicates higher flexibility and lower stiffness of the material. This trend is consistent with the well-established mechanical behavior of $TiB_2$, which exhibits high stiffness due to directional covalent Ti–B bonding.[31] As per the literature reported, $TiB_2$ in general is known to have higher stiffness followed by $HfB_2$, $ZrB_2$, and $VB_2$.[19] The exceptional stiffness demonstrated by some of the HEBs can be attributed to the presence of strong covalent bonding networks, which in turn depend on the concentration and lattice positions of constituent metals and their interaction with boron. Less mismatch of atomic radii of the constituent metals and reduced lattice strain would enable stronger directional bonding and more efficient load transfer. Also, $HfB_2$, $ZrB_2$, and $TiB_2$ rich compositions are known to exhibit high elastic moduli due to their strong M–B bonding and low elastic anisotropy.[32,33]

The influence of metal concentration on the ductility and brittleness of the studied HEBs was analyzed in Fig. 2(c) and (d) by comparing "Poisson's ratio ($\nu$) & Pugh's ratio ($B/G$)" and "Cauchy pressure (CP = $C_{12}$–$C_{44}$) & Pugh's ratio ($B/G$)". Typically, brittle materials show negative Cauchy pressure and $B/G < 1.75$, which means, due to directional covalent bonding, the material could resist volume change under stress and would have less ability to deform before fracture. On the other hand, the ductile materials show positive CP and $B/G > 1.75$, indicating that the intrinsic metallic character due to non-directional metallic bonding results in the material exhibiting resistance to volume change and significant deformation before breaking when under stress.[22,35] The Pugh's ratio and Poisson's ratio of all 18 HEB compositions as plotted in Fig. 2(c) indicate that all the HEB compositions are brittle in nature due to $B/G < 1.5$ (values range between 1.01 and 1.13) and $\nu < 0.25$ (values range between 0.127 and 0.16). Similarly, the CP and $B/G$ as plotted in Fig. 2(d) confirm that all the HEB compositions are brittle in nature due to the negative CP (values in the range of −155 GPa to −115 GPa) and Pugh's ratio $B/G$ being less than 1.75. The less the magnitude of negative CP, the more brittle the material would be due to more angular and directional covalent bonding, signifying the presence of more localized electrons between atoms, suggesting strong electron density along the bond. The Ti rich HEB-4 ($Ti_{0.42}Zr_{0.17}Hf_{0.25}V_{0.17}B_2$) showed the lowest negative CP and $B/G$, suggesting that this composition could be more brittle than the others.

Hardness, by definition, characterizes the ability of a material to resist permanent deformation. Hardness of the HEBs as computed from the empirical equation (eqn (23)) is reported in Fig. 3(a). The hardness of the studied HEBs ranged between 35.72 and 43.22 GPa based on the composition. The equiatomic HEB-1 ($Ti_{0.25}Zr_{0.25}Hf_{0.25}V_{0.25}B_2$) exhibited a hardness of 38.82 GPa. However, the notably highest hardness of 43.22 GPa was exhibited by the Ti rich HEB-4 ($Ti_{0.42}Zr_{0.17}Hf_{0.25}V_{0.17}B_2$). Furthermore, the HEBs having a higher Ti atomic fraction of 0.42 (HEB-2 to HEB-7) showed higher hardness (41–43 GPa) compared to other compositions studied. On the other hand, the HEBs rich in V concentration, such as HEB-8, HEB-9, HEB-11, and HEB-14, showed the lowest hardness (35.5–36.5 GPa). The ultrahigh hardness values (>40 GPa) displayed by the Ti-rich HEBs studied in the present work align with reports of superhard HEBs, where resolidified Ti-rich and lattice-distorted structures resulted in hardness beyond 40 GPa.[13] These observations suggest that increasing $TiB_2$ concentration increased the Ti–B covalent bonds. The resulting localized lattice strain can act as an obstacle to effectively impede plastic deformation to enhance hardness. Furthermore, the hardness signifies the resistance of the material to compression and shear against external force. Typically, in ceramics, due to the shorter bond length resulting from strong interaction and a 2D graphene-like network, the B–B bond imparts resistance to compression, and the M–B bond is responsible for resistance against shear. Therefore, higher concentrations of strong M–B bonds are critical for high hardness.

Fracture toughness ($K_{IC}$) describes the material's resistance to crack propagation during plastic deformation. The value of $K_{IC}$ was computed by using eqn (24) and is shown in Fig. 3(b). The $K_{IC}$ of all the HEBs was in the range of 3.25–3.65 MPa $m^{1/2}$ based on the composition. Among the HEBs studied, the equiatomic HEB-1 ($Ti_{0.25}Zr_{0.25}Hf_{0.25}V_{0.25}B_2$) showed the lowest fracture toughness of 3.25 MPa $m^{1/2}$. Furthermore, among the tuned compositions, the Hf rich HEB-8 ($Ti_{0.08}Zr_{0.25}Hf_{0.42}V_{0.25}B_2$) showed the highest $K_{IC}$ of 3.65 MPa $m^{1/2}$ (Fig. 3(b)). This indicates that, though the equiatomic HEB structure stabilizes in a single phase, it can potentially develop atomic defects and microstructural heterogeneities, which reduce the crack propagation resistance.[37] The highest $K_{IC}$ of 3.65 MPa $m^{1/2}$ was shown by HEB-8 ($Ti_{0.08}Zr_{0.25}Hf_{0.42}V_{0.25}B_2$), which has low Ti and high Hf concentrations. Furthermore, an increase in Ti concentration and a decrease in Hf concentration caused a reduction in the $K_{IC}$ values. For instance, HEB-7 ($Ti_{0.42}Zr_{0.17}Hf_{0.17}V_{0.25}B_2$) and HEB-13 ($Ti_{0.17}Zr_{0.25}Hf_{0.33}V_{0.25}B_2$) showed low $K_{IC}$ (3.63 MPa $m^{1/2}$) compared to HEB-8. This trend suggests that the presence of Hf toughens the ceramic through microstructural refinement and enhanced crack-bridging mechanisms.[38] Additionally, low Ti concentrations may significantly decrease lattice distortion to yield a more favorable microstructure, which aids in resisting the crack propagation. Furthermore, in the case of HEB-6 ($Ti_{0.42}Zr_{0.25}Hf_{0.25}V_{0.08}B_2$) and HEB-17 ($Ti_{0.33}Zr_{0.25}Hf_{0.25}V_{0.17}B_2$), while Zr and Hf were maintained at a concentration of 0.25, it was observed that, when Ti concentration dropped from 0.42 to 0.33 and V increased from 0.08 to 0.17, toughness slightly decreased from 3.63 to 3.65 MPa $m^{1/2}$. This suggests the threshold effect of metal concentration.

The brittleness index (BI), as expressed by eqn (25), is an effective method to quantitatively evaluate the resistance to brittle failure for brittle materials.[36]

$$\mathrm{BI} = \frac{H_\mathrm{V}}{K_\mathrm{IC}} \tag{25}$$

where $H_V$ (GPa) is the Vickers hardness and $K_{IC}$ (MPa $m^{1/2}$) is the fracture toughness. The brittleness index (BI) calculated for the studied HEBs is presented in Fig. 3(c). The unit of BI is $\mu m^{-1/2}$. Among all the HEBs studied, the HEB-8 ($Ti_{0.08}Zr_{0.25}Hf_{0.42}V_{0.25}B_2$),

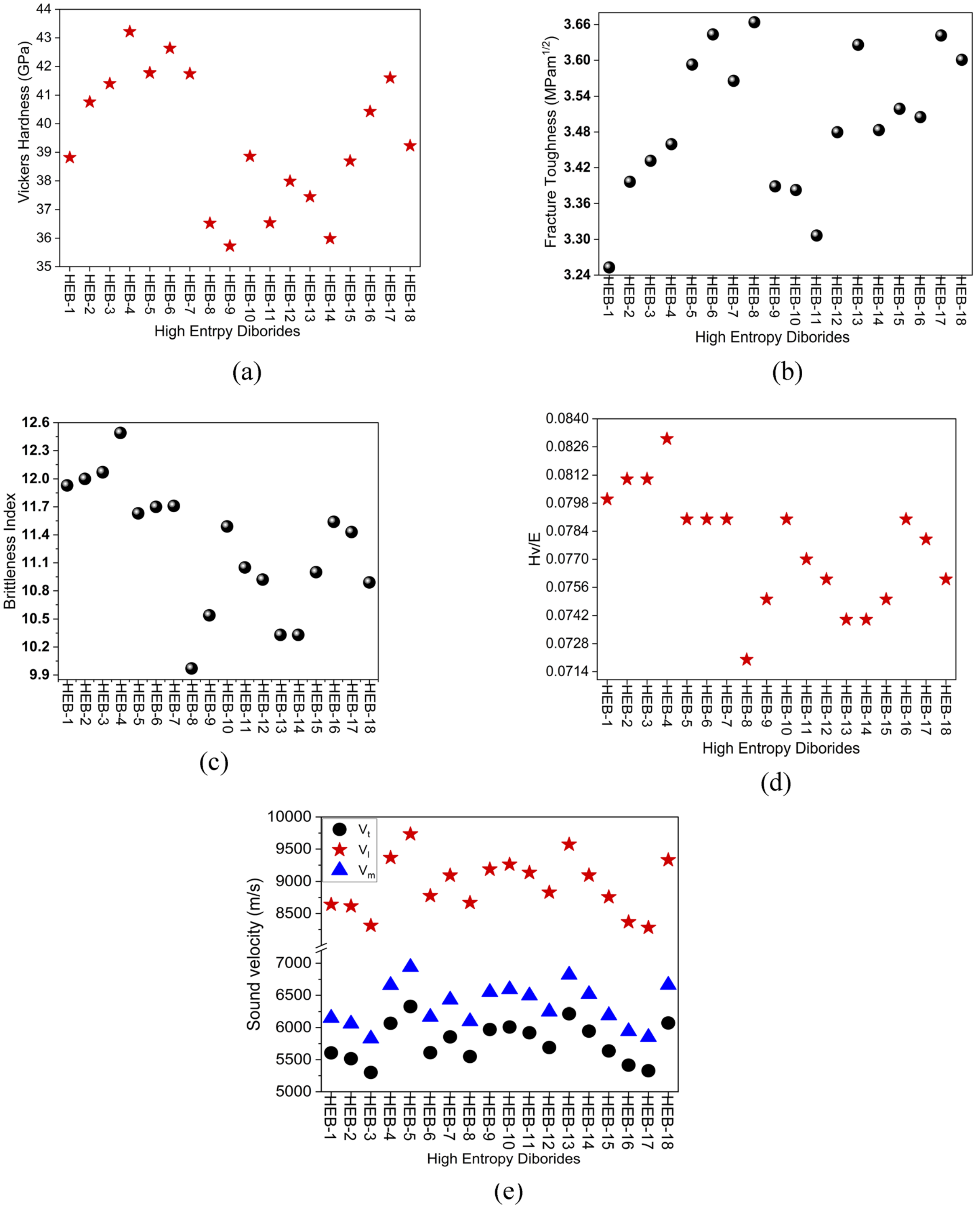

**Fig. 3** Mechanical stability of TiZrHfV-based HEBs: (a) fracture toughness, (b) hardness, (c) brittleness index, (d) wear resistance ($H_V/E$) and (e) sound velocity.

HEB-9 ($Ti_{0.08}Zr_{0.25}Hf_{0.25}V_{0.42}B_2$), HEB-13 ($Ti_{0.17}Zr_{0.25}Hf_{0.33}V_{0.25}B_2$) and HEB-14 ($Ti_{0.17}Zr_{0.25}Hf_{0.25}V_{0.33}B_2$) demonstrated the potential to be less brittle (due to a low brittleness index), while HEB-4 ($Ti_{0.42}Zr_{0.17}Hf_{0.25}V_{0.17}B_2$) followed by HEB-2 ($Ti_{0.42}Zr_{0.25}Hf_{0.08}V_{0.25}B_2$) and HEB-3 ($Ti_{0.42}Zr_{0.25}Hf_{0.17}V_{0.17}B_2$) appeared to show more brittle nature. These trends indicate that the compositions having a high concentration of Ti and a low concentration of V and Hf exhibited more brittleness. The compositions having a low concentration of Ti and a higher concentration of Hf and V exhibited less brittleness. This observation is in correlation with the other brittleness indicators such as Cauchy pressure and Pugh's ratio (Fig. 2(d)).

The mechanical strength of the materials in terms of elastic modulus, fracture toughness, and hardness can be correlated to the lattice volume and density. Density is a function of the portion of the atoms present (contributes to mass) and atomic packing (contributes to lattice parameters and volume). From Fig. 1(b), it can be observed that the HEBs having low lattice volume exhibited low density, and the HEBs having high lattice volume exhibited high density. A comparison of Fig. 1(b) with Fig. 2(b), 3(a) and (b) illustrates that HEBs having low lattice volume and density exhibited higher elastic modulus, higher hardness, but lower fracture toughness. The low lattice volume results from smaller lattice parameters, which are indicative of strong interatomic interactions and shorter bonds, which enable the material to offer great resistance to deformation. On the other hand, the low lattice volume and low density of the material result in reduced availability of the material to absorb energy during fracture, to resist crack propagation.[39] Also, low lattice volume and density offer more pathways for the crack propagation, and therefore the material is prone to fracture.

Feltrin *et al.* reported the experimental investigations of the equiatomic $(Ti_{0.25}V_{0.25}Zr_{0.25}Hf_{0.25})B_2$ HEB and the properties such as hardness (33.2 GPa), elastic modulus (466 GPa), and fracture toughness (4.1 MPa $m^{1/2}$).[14] The present work evaluated various compositions along with the equiatomic composition of Ti, V, Zr, and Hf-based diborides using DFT. The parameters obtained using DFT for equiatomic combination $(Ti_{0.25}V_{0.25}Zr_{0.25}Hf_{0.25})B_2$ are hardness (38.8 GPa), elastic modulus (480 GPa), and fracture toughness (3.24 MPa $m^{1/2}$). This shows that the findings obtained from the DFT calculations in the present work are in good agreement with the experimental investigation reported by Feltrin *et al.* Also, these findings emphasize that, compared to the most widely explored equiatomic composition HECs, there exist other compositions that have the potential to show better properties. Further tuning of elemental concentration could therefore be advantageous to identify materials with optimum composition displaying targeted and enhanced properties.

The resistance of a material to wear could be quantified by the ratio of $H_V/E$ (Fig. 3(d)). Wear resistance is a key performance indicator for materials in extreme environment applications. Higher $H_V/E$ values indicate a good balance between hardness and elastic modulus of a material to display better wear resistance properties.[8] For better wear resistance, it is critical to have a good balance between the material's ability to resist permanent deformation, which is represented by hardness, and the ability of the material to regain its original shape, which is represented by Young's modulus.[9,40,41]

The $H_V/E$ of the studied HEBs as plotted in Fig. 3(d) indicates the superior wear resistance properties of HEB-4 $(Ti_{0.42}Zr_{0.17}Hf_{0.25}V_{0.17}B_2)$ followed by HEB-2 $(Ti_{0.42}Zr_{0.25}Hf_{0.08}V_{0.25}B_2)$, HEB-3 $(Ti_{0.42}Zr_{0.25}Hf_{0.17}V_{0.17}B_2)$, HEB-1 $(Ti_{0.25}Zr_{0.25}Hf_{0.25}V_{0.25}B_2)$, HEB-5 $(Ti_{0.42}Zr_{0.08}Hf_{0.25}V_{0.25}B_2)$, HEB-6 $(Ti_{0.42}Zr_{0.25}Hf_{0.25}V_{0.08}B_2)$ and HEB-7 $(Ti_{0.42}Zr_{0.17}Hf_{0.17}V_{0.25}B_2)$. This trend confirms that the higher concentrations of $TiB_2$ are favorable to achieve higher wear resistance. Therefore, although HEB-4 showed potential to be highly brittle (due to the highest brittleness index), this HEB also showed high hardness and higher stability to wear.

The longitudinal, transverse, and average sound velocities ($\nu_l$, $\nu_t$, and $\nu_M$) of all the HEBs studied are reported in Fig. 3(e). Typically, $\nu_l$ would be higher than $\nu_t$ as the sound propagation in the longitudinal mode is fundamentally faster than the transverse mode.[42] HEB-5 $(Ti_{0.42}Zr_{0.08}Hf_{0.25}V_{0.25}B_2)$ exhibited the highest sound velocity, arising from strong inter-atomic bonding, also indicating the superior stiffness of this composition. Other HEBs such as HEB-4 $(Ti_{0.42}Zr_{0.17}Hf_{0.25}V_{0.17}B_2)$, HEB-13 $(Ti_{0.17}Zr_{0.25}Hf_{0.33}V_{0.25}B_2)$, and HEB-18 $(Ti_{0.33}Zr_{0.17}Hf_{0.25}V_{0.25}B_2)$ also showed higher sound velocity but slightly less than HEB-5.

### 3.3.1. Elastic anisotropy analysis.

Single crystals exhibit elastic anisotropy based on their symmetry and crystal structure. The elastic anisotropy of a crystal is quantified through the "universal elastic anisotropy index" ($A^U$), as per eqn (22).[6,43] A crystal exhibits isotropic nature for "$A^U = 0$", while the deviation from zero designates anisotropy.[44] Typically, mechanical anisotropy in materials is caused by anisotropic atomic bonding, which leads to varied response to mechanical stress in different crystallographic directions.[45] The atomic anisotropy in materials like HEBs is due to the highly disordered arrangement of multiple types of atoms, which further leads to varied chemical bonds and bond strengths, and electron distribution, which further results in different properties in different crystallographic directions.[46]

As the anisotropy significantly affects the mechanical durability and micro-crack behavior of materials, it is critical to evaluate the anisotropy of the material.[42] Fig. 4(a) shows that the HEBs have $A^U$ values in a range of 0.12–0.26, designating the anisotropy of the crystal structures of HEBs. Among the studied HEBs, HEB-10 $(Ti_{0.08}Zr_{0.33}Hf_{0.33}V_{0.25}B_2)$ showed the higher $A^U$ of 0.26, highlighting its strong anisotropic behavior. Typically, HEBs exhibit strong anisotropy due to their $MB_2$-type hexagonal crystal structure, which is made up of closely packed metal atom layers and alternating hexagonal boron layers. This structural configuration causes relatively weaker interlayer interactions and strong in-plane metal–boron (M–B) bonds, which are responsible for the anisotropic behavior seen in HEBs.[13] Furthermore, the anisotropy also arises because of the presence of different types of directional atomic bonding and bond strength due to the presence of different types of metal cations arranged in a highly random manner due to the inherent high entropy.[22]

The directional variations in the elastic properties of HEBs were comprehensively analyzed using an open-source MATLAB code, "AnisoVis".[34] Fig. 4(b)–(g) illustrates the elastic properties along different directions using 2D and 3D profiles. These graphical representations illustrate how Young's modulus, linear compressibility, shear modulus, and Poisson's ratio vary in different plane projections and directions. The maximum and minimum values of each modulus indicate the level of anisotropy present in the HEBs, which allows for the identification of directions (coordinates) of interest in the elastic properties that are not always parallel to the crystallographic axes of the material.[34] The 3D projections in *xy*, *yz*, and *xz*

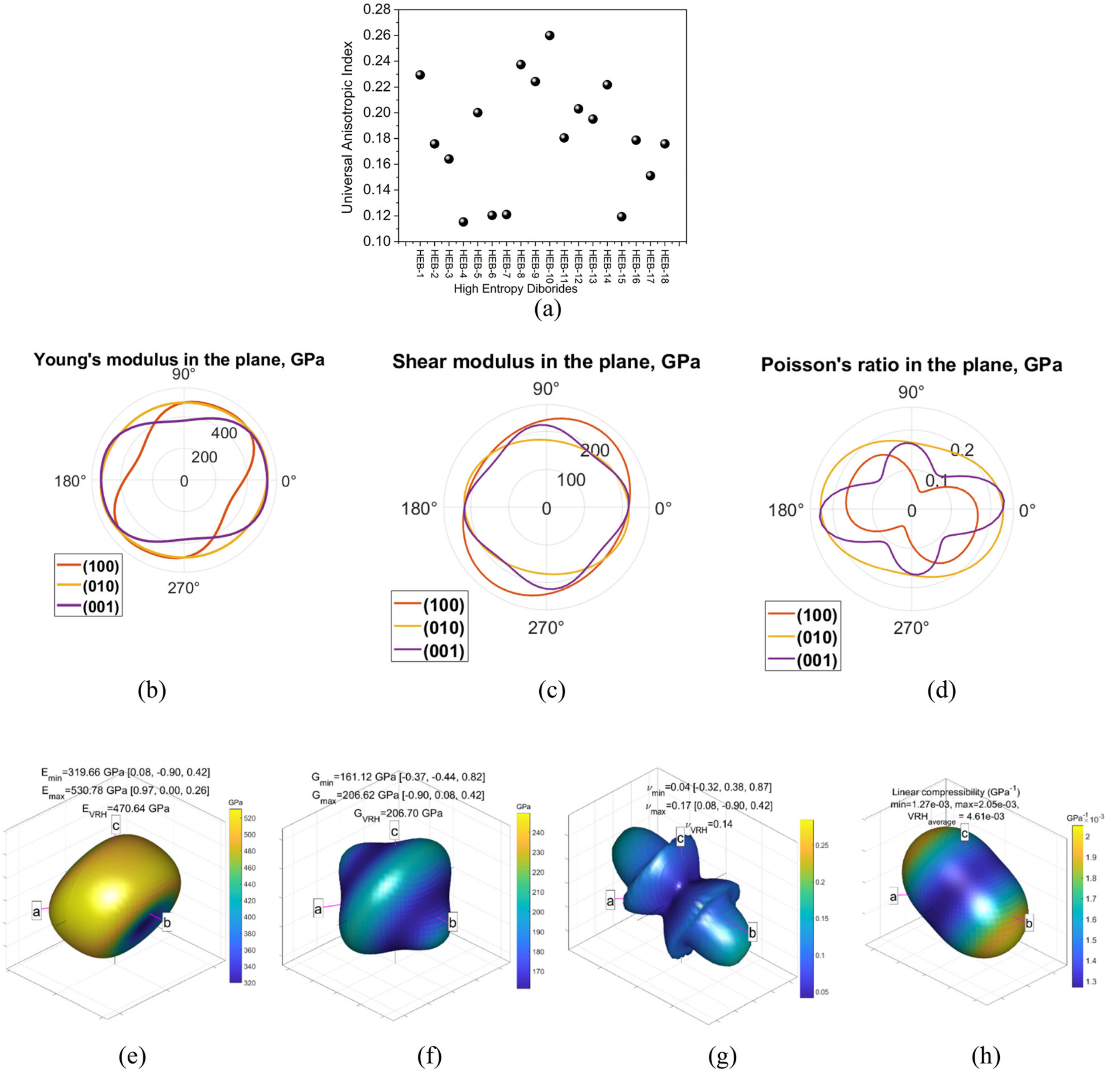

Fig. 4 (a) Anisotropy in elastic moduli of HEBs, (b) 2D profiles of Young's modulus of HEB-1 ($Ti_{0.25}Zr_{0.25}Hf_{0.25}V_{0.25}B_2$), (c) 2D profiles of shear modulus of HEB-1, (d) 2D profiles of Poisson's ratio of HEB-1, (e) 3D profile of Young's modulus of HEB-1, (f) 3D profile of shear modulus of HEB-1, (g) 3D profile of Poisson's ratio of HEB-1, and (h) 3D profile of linear compressibility of HEB-1.

planes reveal the presence of increased anisotropy in Young's modulus, linear compressibility, shear modulus, and Poisson's ratio. For an isotropic crystal, the 3D projections will take a perfect spherical shape. Fig. 4 and S2 of SI confirm that all the HEBs display elastic anisotropy. These figures shed important light on the intricate directional dependence of elastic properties within structures and contribute significantly to our understanding of mechanical behavior. The anisotropy in these HEBs is also due to the lattice distortions. Furthermore, it was observed that for all the HEBs, the anisotropy in shear modulus was higher than the anisotropy in Young's modulus, which suggests that HEBs are more anisotropic in certain non-axial directions of the crystal. The anisotropy in linear compressibility was more significant in the (0 0 1) direction than that in the (1 0 0) and (0 1 0) directions. Overall, a strong directional bonding dependency was observed in the HEBs, which shows their mechanical performance, such as deformation behavior, crack resistance, *etc.*, depending on the loading direction.

### 3.4. Thermodynamic properties

Debye temperature ($\Theta_D$), a characteristic temperature derived from the Debye model, is an important thermodynamic property that is correlated to properties such as thermal conductivity, specific heat, vacancy formation energy, and thermal expansion coefficient. The Debye temperature of HEBs was calculated as a function of acoustic velocity as per eqn (18)[47] and is presented in Fig. 5(a).

The $\Theta_D$ signifies the maximum frequency of lattice vibrations, which results from the strength of interatomic bonds. Low Debye temperature of a material results from weak interatomic bond strength, and the material will have more low-frequency vibrational modes. Therefore, their atoms exhibit easy vibrations even with low energy, which lead to high specific heats at low temperatures. Furthermore, weak interatomic bonding results in more scattered phonons, which further results in low thermal conductivity. On the other hand, materials having high Debye temperatures exhibit high thermal conductivity due to the presence of strong interatomic bonds and their atoms need more energy for easy vibrations.[48] Furthermore, as $C_V \propto \frac{T}{{\theta_D}^3}$, at higher temperatures ($T \gg \Theta_D$), materials with low Debye temperature would exhibit high specific heat and the materials with high Debye temperature exhibit low specific heat. As the Debye temperature is proportional to mean sound velocity, the Debye temperature followed the same trend as sound velocity. For instance, HEB-5 ($Ti_{0.42}Zr_{0.08}Hf_{0.25}V_{0.25}B_2$) showed the highest sound velocity as well as higher $\Theta_D$ (Fig. 5(a)). Most of the non-equiatomic HEBs showed higher $\Theta_D$ compared to the equiatomic HEB-1 (Fig. 5(a)). HEB-4 ($Ti_{0.42}Zr_{0.17}Hf_{0.25}V_{0.17}B_2$), HEB-5 ($Ti_{0.42}Zr_{0.08}Hf_{0.25}V_{0.25}B_2$), HEB-13 ($Ti_{0.17}Zr_{0.25}Hf_{0.33}V_{0.25}B_2$), and HEB-18 ($Ti_{0.33}Zr_{0.17}Hf_{0.25}V_{0.25}B_2$) showed higher $\Theta_D$, indicating stronger interatomic bonding and enhanced lattice stiffness, which translates to superior mechanical strength, thermal stability, and low thermal conductivity. This high $\Theta_D$ suggests reduced vibrations of atoms at a given temperature, which indicates strong bonding, a stiff lattice, along with improved elastic moduli, and higher resistance to thermal shock, which are key traits for ultra-high temperature applications. It was observed that the HEBs showing high sound velocity and Debye temperature are low in zirconium concentrations compared to other constituent elements.

The melting points of the HEBs as computed using the empirical equation (eqn (5)) are presented in Fig. 5(b). Since the HEBs studied are relatively cubic, the $C_{11}$ used in eqn (5) was computed as $C_{11} = (C_{11} + C_{22} + C_{33})/3$. All the non-equiatomic HEBs showed higher melting points than the equiatomic HEB-1. HEB-17 ($Ti_{0.33}Zr_{0.25}Hf_{0.25}V_{0.17}B_2$) exhibited the highest melting point of 3934 K. The lowest melting point of 3465 K was exhibited by HEB-10 ($Ti_{0.08}Zr_{0.33}Hf_{0.33}V_{0.25}B_2$). Broadly, it can be observed that the highest melting points were shown by those HEB configurations that had higher concentrations of titanium and hafnium. Further observations include: (i) for a fixed Zr and Hf concentration, increase in Ti and decrease in V concentration have increased the melting point, (ii) for a fixed Zr and V concentration, decrease in Ti and increase in Hf concentration have improved the melting point, and (iii) for a fixed Ti and V concentration, increase in Hf concentration has improved the melting point. Therefore, it can be concluded broadly that Ti and Hf concentrations have relatively more influence on the melting point of the studied HEBs.

### 3.5. Electronic properties

**3.5.1. Density of states.** The structural stability of the HEB structures was evaluated by analyzing the total density of states (DOS) of the electronic structures. Fig. 6(a) and (b) show the equiatomic HEB crystal structure and its total DOS. The total DOS of equiatomic HEB-1, along with the projected DOS of constituent cations of HEB, such as Ti, Zr, Hf, V, and anion B, is shown in Fig. 6(b). The DOS of the remaining 17 HEB compositions is presented in the S3, SI.

The lattice distortion, which causes significant lattice strain, typically arises from the random distribution of multiple transition-metal cations having different atomic radii in the HEB structure (Fig. 6(a) for equiatomic HEB-1). The lattice distortion causes variation in local bonding environments

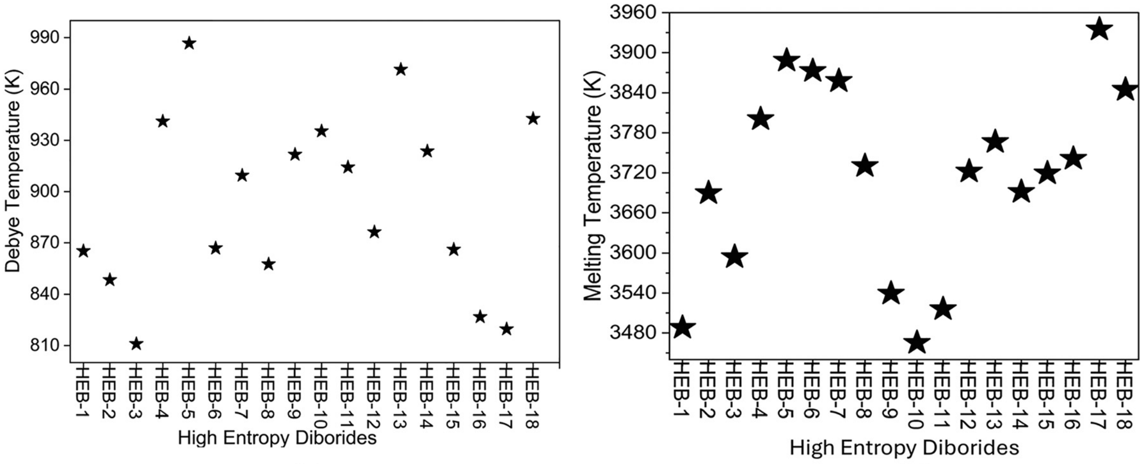

(a) (b)

Fig. 5 Thermodynamic properties of Ti, Zr, Hf and V based HEBs: (a) Debye temperature and (b) melting point.

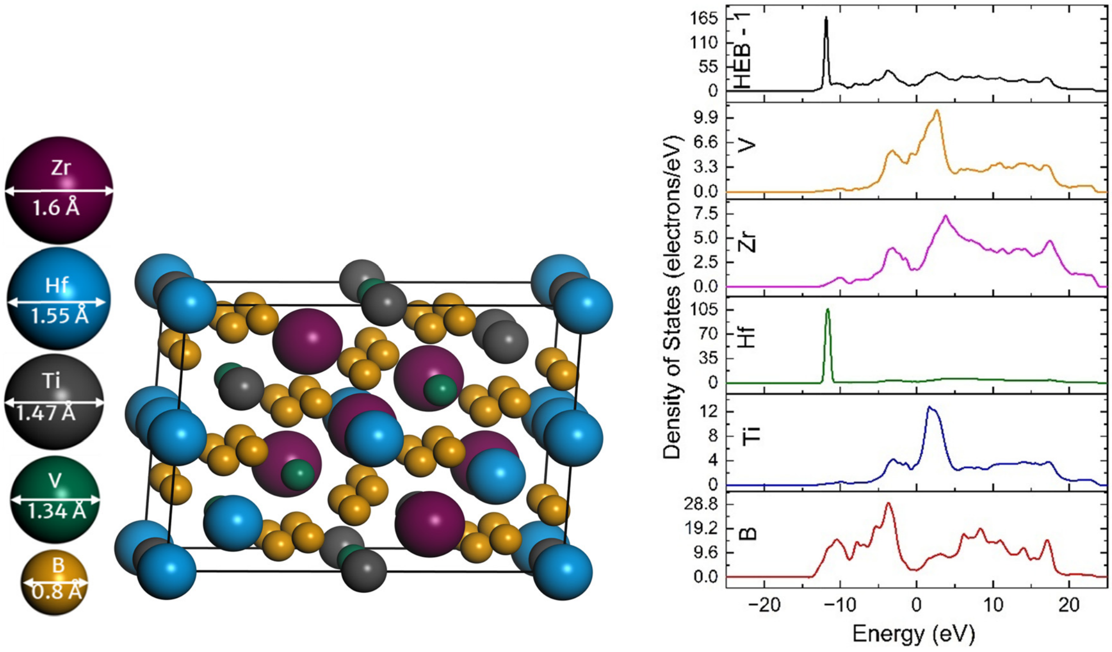

(a) (b)

Fig. 6 Equiatomic (TiZrHfV)$B_2$ HEB-1: (a) crystal structure, (b) total density of states of HEB-1 and the projected density of states of constituent elements.

and enhances the orbital overlap between the d-states of metal atoms and p-states of boron by reducing symmetry and altering bond lengths between atoms, which enable stronger and directional bonds. This is reflected in the broadened bonding peaks and the formation of the pseudo-gap near the Fermi level in the DOS (Fig. 6(b)). The total DOS of equiatomic HEB-1 (Fig. 6(b)) shows a non-zero density of states at the Fermi level, indicating available electron energy states, suggesting possible superconductivity. Furthermore, a valley at $-1.08$ eV near the Fermi level (pseudo-gap) resulting from the hybridization of the d-orbital of metal atoms and p-orbital of boron atoms was observed. This pseudo-gap confirms the presence of covalent bonds in the material. The bonding states formed from the d-orbital of metal and the p-orbital of boron occurred at $-13.80$ eV, and the antibonding states were above the Fermi level. Two bonding peaks were observed at $\sim -11.86$ eV and $-3.62$ eV. The peak at $-11.86$ eV was observed to be due to the hybridization of d–p orbitals of Hf and B, respectively. The peak at $-3.62$ eV was observed to be due to the hybridization of d–p orbitals of Ti, Zr, and V with B. The metals such as Ti, Zr, and V showed a relatively higher DOS at the Fermi level, indicating weaker covalent bonds with boron (Fig. 6(b)). On the other hand, Hf had a low DOS (1.65) at the Fermi level, indicating stronger covalent bonding with boron, signifying the higher contribution of Hf–B bonds to mechanical stiffness and hardness. The strong Hf–B bond strength can also be confirmed from the higher Hf–B bond population (Table 3) associated with its local coordination and bond shortening within the distorted lattice. For the studied HEBs, based on the composition, the bonding states occurred in the range of $-12.3$ eV to $-14.2$ eV, while the peak of bonds was observed at around $\sim -12.00$ eV and $-3.86$ eV for all the HEBs. Thus, the structural disorder and lattice distortion directly influence the electronic hybridization, the position and width of bonding states, and the pseudo-gap formation, which in turn governs the bonding strength and mechanical stability of the HEBs. The DOS of all the HEBs is presented in S3, SI.

**3.5.2. Structural stability.** The structural stability of the materials can be assessed through the band-filling theory. The band-filling theory states that the bonding states, particularly for p–d covalent compounds, can be used to predict the structural stability of a crystal.[49,50] A crystal structure is considered to be stable when it is in its lowest overall energy state. The electron distribution in the covalent bonds of a ceramic crystal and the nature of electrons in the bonding states (localized/delocalized) govern the lowering of the energy state of the crystal. In this regard, the structural stability of the HECs was calculated from the stability ratio as defined in eqn (26).

$$\text{Stability ratio} = \frac{W_{\text{occ}}}{W_{\text{b}}} \tag{26}$$

where $W_{\text{occ}}$ denotes the width of occupied states (energy range in the DOS measured as the distance from the bottom of the bonding states to the Fermi level $E_{\text{F}}$) and $W_{\text{b}}$ denotes the width of bonding states (energy range in the DOS measured as the distance from the bottom of the bonding states to the pseudo gap, which is the dip in DOS before antibonding states begin). Typically, $\frac{W_{\text{occ}}}{W_{\text{b}}} \approx 1$ indicates that all bonding states are fully filled, implying maximum structural stability. $\frac{W_{\text{occ}}}{W_{\text{b}}} > 1$ indicates that the electrons spill into anti-bonding states,

Table 2 Width of occupied states ($W_{\mathrm{occ}}$) and bonding state width ($W_{\mathrm{b}}$), stability ratio $\left(\frac{W_{\mathrm{occ}}}{W_{\mathrm{b}}}\right)$, average M–B bonding energy ($W_{\mathrm{pd}}$) and the number of valence electrons for Ti, Zr, Hf and V based HEBs

| Code | HEC | $W_{\mathrm{occ}}$ (eV) | $W_{\mathrm{b}}$ (eV) | $W_{\mathrm{occ}}/W_{\mathrm{b}}$ | $W_{\mathrm{pd}}$ (eV) | $n_{\mathrm{b}}$ |
|---|---|---|---|---|---|---|
| HEB-1 | $Ti_{0.25}Zr_{0.25}Hf_{0.25}V_{0.25}B_2$ | 13.8 | 12.6 | 1.10 | 2.06 | 335.97 |
| HEB-2 | $Ti_{0.42}Zr_{0.25}Hf_{0.08}V_{0.25}B_2$ | 13.0 | 11.5 | 1.13 | 2.27 | 286.27 |
| HEB-3 | $Ti_{0.42}Zr_{0.25}Hf_{0.17}V_{0.17}B_2$ | 12.3 | 11.3 | 1.09 | 2.61 | 339.70 |
| HEB-4 | $Ti_{0.42}Zr_{0.17}Hf_{0.25}V_{0.17}B_2$ | 14.0 | 13.1 | 1.07 | 2.38 | 342.13 |
| HEB-5 | $Ti_{0.42}Zr_{0.08}Hf_{0.25}V_{0.25}B_2$ | 14.0 | 12.8 | 1.09 | 2.64 | 342.13 |
| HEB-6 | $Ti_{0.42}Zr_{0.25}Hf_{0.25}V_{0.08}B_2$ | 13.6 | 13.1 | 1.04 | 1.82 | 333.54 |
| HEB-7 | $Ti_{0.42}Zr_{0.17}Hf_{0.17}V_{0.25}B_2$ | 14.2 | 13.2 | 1.08 | 2.62 | 315.72 |
| HEB-8 | $Ti_{0.08}Zr_{0.25}Hf_{0.42}V_{0.25}B_2$ | 13.8 | 12.8 | 1.08 | 2.28 | 393.59 |
| HEB-9 | $Ti_{0.08}Zr_{0.25}Hf_{0.25}V_{0.42}B_2$ | 13.8 | 12.4 | 1.11 | 2.15 | 337.99 |
| HEB-10 | $Ti_{0.08}Zr_{0.33}Hf_{0.33}V_{0.25}B_2$ | 13.6 | 12.6 | 1.08 | 1.81 | 364.40 |
| HEB-11 | $Ti_{0.08}Zr_{0.25}Hf_{0.33}V_{0.33}B_2$ | 13.8 | 12.6 | 1.10 | 2.40 | 365.82 |
| HEB-12 | $Ti_{0.08}Zr_{0.33}Hf_{0.25}V_{0.33}B_2$ | 13.8 | 12.6 | 1.10 | 2.05 | 340.23 |
| HEB-13 | $Ti_{0.17}Zr_{0.25}Hf_{0.33}V_{0.25}B_2$ | 13.8 | 12.8 | 1.08 | 2.06 | 364.33 |
| HEB-14 | $Ti_{0.17}Zr_{0.25}Hf_{0.25}V_{0.33}B_2$ | 13.7 | 12.4 | 1.10 | 2.25 | 338.49 |
| HEB-15 | $Ti_{0.17}Zr_{0.33}Hf_{0.25}V_{0.25}B_2$ | 13.7 | 12.7 | 1.08 | 2.16 | 340.23 |
| HEB-16 | $Ti_{0.33}Zr_{0.25}Hf_{0.17}V_{0.25}B_2$ | 13.9 | 12.7 | 1.10 | 2.02 | 310.45 |
| HEB-17 | $Ti_{0.33}Zr_{0.25}Hf_{0.25}V_{0.17}B_2$ | 13.7 | 12.8 | 1.07 | 1.93 | 334.61 |
| HEB-18 | $Ti_{0.33}Zr_{0.17}Hf_{0.25}V_{0.25}B_2$ | 13.9 | 12.9 | 1.08 | 2.25 | 340.49 |

which reduces stability. When $\frac{W_{\mathrm{occ}}}{W_{\mathrm{b}}} < 1$, some bonding states are unfilled, leading to reduced stability.[50] Using band-filling theory, the structural stability of the studied HEBs was assessed by examining $\frac{W_{\mathrm{occ}}}{W_{\mathrm{b}}}$, as shown in Table 2. Greater phase stability is indicated by values closer to 1, which also suggests optimal filling of bonding states. The average M–B bonding energy $W_{\mathrm{pd}}$ is evaluated as the distance from the bottom of the band to the main peak of the bonding states (M-d–B-p overlap). The number of valence electrons ($n_{\mathrm{b}}$) of the HEBs is calculated by integrating the total DOS against the energy from the lowest energy state in the valence bond up to the Fermi level. For all the HEBs studied, the computed values of $W_{\mathrm{pd}}$, $W_{\mathrm{occ}}$, $W_{\mathrm{b}}$ and $\frac{W_{\mathrm{occ}}}{W_{\mathrm{b}}}$ are shown in Table 2.

In Table 2, the $W_{\mathrm{occ}}$ value was observed to lie in the range of 12.3 to 14.2, and the $W_{\mathrm{b}}$ value was in the range of 11.3 to 13.2 for various concentrations of constituent metals. However, except for HEB-2, HEB-3, HEB-4, HEB-5, and HEB-7, all the other HEBs showed nearly the same values of $W_{\mathrm{occ}}$ (13.8), $W_{\mathrm{b}}$ (12.6) and $\frac{W_{\mathrm{occ}}}{W_{\mathrm{b}}}$ (1.08). It was observed that the outlier HEBs (HEB-2, HEB-3, HEB-4, HEB-5, and HEB-7) have higher Ti concentrations than the others. The $W_{\mathrm{occ}}$ and $W_{\mathrm{b}}$ were observed to be narrower for HEB-3 and wider for HEB-7. The $\frac{W_{\mathrm{occ}}}{W_{\mathrm{b}}}$ of all the HEBs being greater than '1' indicates that the bonding states of the HEBs have no room to accommodate the valence electrons. For example, $\frac{W_{\mathrm{occ}}}{W_{\mathrm{b}}} = 1.09$ means only 91% of the valence electrons can be accommodated in bonding states, and the remaining 9% would spill into the non-bonding states, which typically are high-energy states, inducing some structural instability. HEB-6 ($Ti_{0.42}Zr_{0.25}Hf_{0.25}V_{0.08}B_2$) had the lowest ratio of 1.04 among all the compositions (Table 2), suggesting that its bonding states are almost completely occupied with negligible electron spillover into non-bonding states, making it the most stable configuration. HEB-2 ($Ti_{0.42}Zr_{0.25}Hf_{0.08}V_{0.25}B_2$), and HEB-9 ($Ti_{0.08}Zr_{0.25}Hf_{0.25}V_{0.42}B_2$), on the other hand, displayed the highest ratios of 1.13 and 1.11, respectively. This signifies higher electron spill over to non-bonding states, which highlights decreased structural stability. Although the extent varied with composition, most of the systems showed $\frac{W_{\mathrm{occ}}}{W_{\mathrm{b}}}$ ratios that were marginally greater than '1', indicating partial occupation of non-bonding orbitals.

The Ti-rich and V-rich variants had a shift of the Fermi level ($E_{\mathrm{F}}$) further into non-bonding states, reducing their structural robustness, whereas compositions that were equiatomic or nearly equiatomic generally displayed better band-filling characteristics because of balanced d-orbital contributions from multiple elements. According to this analysis, adjusting the elemental ratios can have a major impact on the electronic structure and, consequently, the structural stability of HEBs. Furthermore, HEB-2, HEB-3, HEB-4, HEB-5, and HEB-7, which showed distinct properties compared to the other nine HEBs, have also shown relatively higher average M–B bond energies ($W_{\mathrm{pd}}$) (Table 2). In addition, an increase in the number of valence electrons ($n_{\mathrm{b}}$) did not show any widening of the width of bonding states ($W_{\mathrm{b}}$), indicating that the bonding states do not have additional room to accommodate the valence electrons further. Between HEB-2 (lowest $n_{\mathrm{b}}$) and HEB-16 (second lowest $n_{\mathrm{b}}$), an increase in valence electrons has slightly widened the $W_{\mathrm{b}}$. However, after this, the width of $W_{\mathrm{b}}$ was almost constant (∼12.6 eV). Between HEB-14 ($n_{\mathrm{b}} = 338.5$) and HEB-3 ($n_{\mathrm{b}} = 339.7$), an increase in valence electrons has slightly reduced $W_{\mathrm{b}}$ from 12.6 to 11.3. Comparing HEB-2 and HEB-3, it can be observed that these two Ti-rich compositions have low $W_{\mathrm{b}}$ values. The common aspect of HEB-2 and HEB-3 is that these two HEBs have the same combined concentration of Hf and V (0.34) and the same Ti and Zr concentrations of 0.42 and 0.25, respectively. Table 2 also presents another interesting aspect about HEB-2, HEB-3, HEB-4, HEB-6, and HEB-7, which showed slightly deviated $W_{\mathrm{b}}$, and $W_{\mathrm{pd}}$. These five HEBs have the same Ti concentration of 0.42, and the other three metals, Zr, Hf, and V, follow a peculiar concentration combination, *i.e.* sum of concentrations of any two elements is 0.34.

### 3.5.3. Partial charge analysis and bond population analysis.

The atomic bonding properties of HEBs were assessed through Mulliken charges and bond populations.[47] The Mulliken partial charge and bond population analysis of the equiatomic HEB-1 are presented in Fig. 7(a) and (b), respectively. The same analysis for the rest of the 17 HEBs is presented in the S4 and S5, SI respectively. The charge density of individual atoms in complex systems such as high entropy ceramics is greatly influenced by the local atomic environment because of the presence of different types of interatomic interactions and structural configurations. The interatomic interactions directly govern the compound strength, flexibility, thermal conductivity, and energy storage capacity of the material. As per the Mulliken partial charge distribution of equiatomic HEB-1 presented in Fig. 7(a) and other HEBs in the S4, SI, the partial charges on the metal atoms in all compositions ranged roughly from +0.8 to +1.4, whereas the partial charge on boron atoms ranged between −0.58 and −0.60, indicating the significant role of metal–boron (M–B) bonding in the overall electronic structure. This highlights the mixed ionic–covalent nature of the bonding in these compositions by showing a significant charge transfer from metal atoms to boron.

Compared to different metals (Ti, Zr, Hf, and V), the degree of charge dispersion between individual atoms of a particular metal type appears to be less pronounced. This highlights the stabilization of the local bonding environment by suggesting a more consistent interaction strength between atoms of the same element. Furthermore, the Zr atoms showed the highest positive charge (highest oxidation states) compared to other metals in all the HEBs, which means that, due to losing more electrons, the shared electron density between the Zr–B covalent bond got reduced. This results in weaker directional Zr–B covalent bond interactions. Conversely, the Hf atoms showed the lowest positive charge among all the HEBs, which signifies stronger Hf–B interactions. The higher charge transfer of Hf–B compared to Zr–B bonds could be attributed to the higher electronegativity difference between Hf and B compared to Zr and B. As per the partial DOS analysis, the electron transfer involving the B atoms is primarily concentrated in the s and p orbitals, while for the metal atoms, it predominantly occurs in the d orbitals.

This illustrates that charges on all metals and boron are delocalized throughout all the designed compositions because partial charges of metals varied from a range of 0.8*e* up to 1.4*e*. By a combined analysis of partial charges and bond populations (Fig. 7(a) and (b)), it becomes evident that the HEB compositions significantly enhanced the ionic character of the Zr–B chemical bond, while Ti–B, Hf–B, V–B, and Zr–B predominantly retain their covalent bonding characteristics. In addition, the weakest bond plays a determinative role in the hardness of materials.[51] Gao *et al.* proposed that bonding strength and the number of bonds per unit area are the two important factors affecting the intrinsic hardness of a covalent material.[24] The bond population of the Zr–B bond is the smallest among all and varies with the tuning of the composition. This implies that the intrinsic hardness of various HEBs will vary as well, following the same general pattern proposed by Tian's correlation.[26] The delocalization of electrons, which is suggestive of metallic behavior in all investigated HEBs, was confirmed by the steady charge transfer from metals to boron with the finite DOS at the Fermi level. The DOS close to the Fermi level indicates the density of free charge carriers available to conduction, whereas partial charge sheds light on the degree and direction of charge transfer as well as the bonding

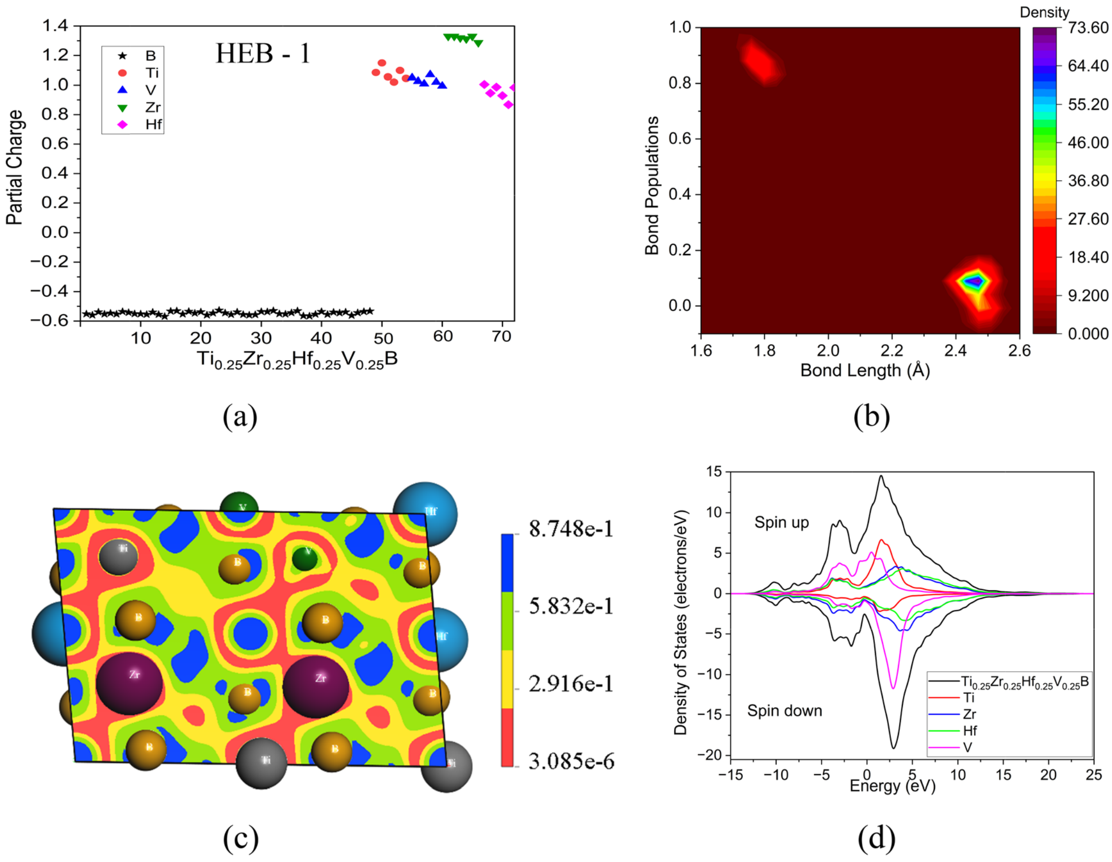

Fig. 7 Electronic properties of HEB-1 ($Ti_{0.25}Zr_{0.25}Hf_{0.25}V_{0.25}B_2$): (a) Mulliken partial charge analysis, (b) bond population, (c) electron localization function (ELF), and (d) spin-up and spin-down d-orbital density of states.

type (ionic, covalent, or metallic), which influences the mechanical strength of the material.

Mulliken bond population, which represents the overlap and strength of atomic orbitals, provides an understanding of bond strength and covalency.[47] The bond population *versus* bond length data for the equiatomic HEB-1 are presented in Fig. 7(b) and for the other 17 HEBs are presented in the S5, SI. The average Mulliken bond population and bond length of B–B, Ti–B, Hf–B, V–B, and Zr–B are presented in Table 3. HEBs with higher bond populations are typically more structurally stable and resistant to mechanical or thermal degradation, making them ideal for hard coatings or high-temperature structural materials. Conversely, HEBs with lower bond populations indicate weaker interactions, which may result in decreased mechanical strength but occasionally increased ionic mobility, which would be a benefit in solid-state batteries or ionic conductors. From Fig. 7(b), Table 3, and S5, SI, it can be seen that the average bond length of B–B, Ti–B, Hf–B, V–B, and Zr–B ranged between 1.76–1.81 Å, 2.40–2.48 Å, 2.46–2.50 Å, 2.42–2.50 Å, and 2.46–3.00 Å, respectively. Furthermore, the bond population followed the order of B–B (0.88) > Hf–B (0.11) > Ti–B (0.08) > V–B (0.07) > Zr–B (−0.02).

The highest B–B bond population indicates strong covalent character, and the B–B region has a strong redistribution of electron density, which can result in boron atoms having a 2D graphene-like network in the crystal. Furthermore, the low metal–boron bond population indicates the weak electron population and ionic–covalent nature of the bond. In almost all of the HEBs, the Zr–B bond showed the lowest and negative bond population, which signifies the transfer of electrons to antibonding orbitals, due to which the Zr–B bond gets weakened or destabilized. Furthermore, the Hf–B bond having the highest bond population among the four metal–boron bonds is the strongest and stable bond, followed by the Ti–B bond. This reveals that the concentrations of Hf and Ti would highly affect various mechanical and thermal properties of the HEBs. This observation gets strong support from the trends of various mechanical and thermal properties discussed in the previous sections.

### 3.5.4. Electron localization function.

The mechanical, thermodynamic, and microstructure characteristics of the materials, from the electron outlook, depend significantly on the nature of the chemical bonds present. The nature of chemical bonding and charge transfer characteristics of a material can be qualitatively represented by the electron localization function (ELF).[50,52] The ELF for the equiatomic HEB-1 is presented in Fig. 7(c), and the ELF of the other 17 HEBs is presented in the S6, SI. The scale of the graphs ranges from approximately zero (red), referring to electron delocalization. Furthermore, the ELF moves towards 0.3 (yellow) and 0.6 (green), and then the ELF reaches close to 1, having an almost 0.87 (blue) value, showing a localized electron region and perfect covalent bonding.

It is clearly seen in all the ELF graphs (Fig. 7(c) and S6, SI) that more charge was localized near boron atoms, highlighted in blue and green colors (ELF ≈ 0.6 to 0.9). This indicates the covalent bonding of B–B and ionic–covalent bonding between metal and boron. On the other hand, a delocalized and nearly homogeneous electron gas around metal atoms was observed, which is highlighted in yellow color (ELF ≈ 0.3). This indicates a weak metallic bonding between the metals. This observation is also supported by Mulliken partial charge analysis and PDOS of atoms. As the molecular orbitals of HEBs have a major contribution from d-orbitals of metals, the Fermi level in the DOS is mainly from d-orbitals. Therefore, it can be confirmed that the ELF, Mulliken, and DOS/PDOS follow the same trend. When the various compositions of studied HEBs were compared, the distribution of ELF, bond population, and average partial charge varied greatly depending on the concentration of the individual metals. This variation is crucial in determining the suitability of any particular HEB composition for various applications.

Low average partial charges imply less charge separation and more uniform electron distribution, which characterizes

Table 3 Average bond population (*P*) and bond length (*L*) of Ti, Zr, Hf and V based HEBs

| | B–B | | B–Hf | | B–Ti | | B–V | | B–Zr | |
|---|---|---|---|---|---|---|---|---|---|---|
| Nomenclature | *P* | *L* | *P* | *L* | *P* | *L* | *P* | *L* | *P* | *L* |
| HEB-1 | 0.88 | 1.76 | 0.11 | 2.49 | 0.08 | 2.40 | 0.07 | 2.45 | −0.02 | 2.49 |
| HEB-2 | 0.87 | 1.77 | 0.11 | 2.47 | 0.08 | 2.43 | 0.07 | 2.43 | −0.03 | 2.46 |
| HEB-3 | 0.86 | 1.78 | 0.11 | 2.47 | 0.09 | 2.44 | 0.07 | 2.43 | −0.02 | 2.48 |
| HEB-4 | 0.86 | 1.78 | 0.10 | 2.47 | 0.08 | 2.44 | 0.07 | 2.44 | −0.03 | 2.47 |
| HEB-5 | 0.86 | 1.77 | 0.09 | 2.46 | 0.07 | 2.43 | 0.06 | 2.42 | −0.05 | 2.47 |
| HEB-6 | 0.85 | 1.79 | 0.10 | 2.48 | 0.08 | 2.45 | 0.07 | 2.44 | −0.03 | 2.48 |
| HEB-7 | 0.86 | 1.78 | 0.09 | 2.46 | 0.08 | 2.43 | 0.07 | 2.42 | −0.04 | 2.46 |
| HEB-8 | 0.85 | 1.80 | 0.11 | 2.50 | 0.09 | 2.47 | 0.06 | 2.47 | −0.01 | 2.51 |
| HEB-9 | 0.87 | 1.78 | 0.11 | 2.48 | 0.08 | 2.45 | 0.07 | 2.46 | −0.01 | 2.49 |
| HEB-10 | 0.85 | 1.80 | 0.12 | 2.50 | 0.09 | 2.48 | 0.07 | 2.48 | −0.003 | 2.50 |
| HEB-11 | 0.86 | 1.79 | 0.12 | 2.49 | 0.07 | 2.47 | −0.01 | 2.50 | 0.08 | 3.00 |
| HEB-12 | 0.86 | 1.79 | 0.12 | 2.49 | 0.09 | 2.46 | 0.07 | 2.46 | −0.01 | 2.49 |
| HEB-13 | 0.85 | 1.79 | 0.11 | 2.49 | 0.09 | 2.46 | 0.07 | 2.46 | −0.02 | 2.49 |
| HEB-14 | 0.86 | 1.79 | 0.11 | 2.48 | 0.09 | 2.46 | 0.07 | 2.45 | −0.01 | 2.49 |
| HEB-15 | 0.86 | 1.79 | 0.12 | 2.49 | 0.09 | 2.47 | 0.07 | 2.46 | −0.01 | 2.49 |
| HEB-16 | 0.86 | 1.78 | 0.11 | 2.47 | 0.09 | 2.44 | 0.07 | 2.46 | −0.02 | 2.47 |
| HEB-17 | 0.85 | 1.79 | 0.11 | 2.48 | 0.09 | 2.45 | 0.07 | 2.44 | −0.02 | 2.48 |
| HEB-18 | 0.83 | 1.81 | 0.10 | 2.47 | 0.08 | 2.43 | 0.06 | 2.43 | −0.03 | 2.47 |

metallic bonding (Fig. 7(a) and S4, SI). High partial charges indicate stronger and more directional bonding, which is associated with covalent or ionic character (Fig. 7(a) and S4, SI). A strong bonding (ionic or covalent), which is associated with high ELF values between atoms, leads to high hardness, thermal stability, and localized chemical interactions, all of which are advantageous for solid electrolytes, protective coatings, and refractory materials. Conversely, metallic bonding behavior is associated with lower ELF values, which indicate delocalized electron density. This supports electrical and thermal conductivity, which is desirable in conductive ceramics, electrodes, or thermoelectric materials. Certain HEB compositions in this study showed a mixed bonding character with moderate partial charges, bond populations, and ELFs. This suggests that they may provide a balance of properties, including both functional performance and mechanical robustness (*e.g.*, in multifunctional structural-electronic components). To customize their behavior and optimize their composition for any particular application, it is crucial to examine how partial charge, bond population, and ELF interact across various compositions.

**3.5.5. Magnetism and spin polarization.** Spin-polarized metals are of great technological importance as they have diverse fields of applications, ranging from spintronic devices to quantum computation.[53] The electronic structure provides the foundational knowledge about the micro-mechanisms of structural stability and mechanical properties. Similarly, the density of states (DOS) provides an understanding of the electrical and optical properties of a system. The ratio of spin polarization can be expressed by means of the spin-up and spin-down DOS around the Fermi level, $E_F$:[54]

$$P = \frac{D^{\uparrow}(E_F) - D^{\downarrow}(E_F)}{D^{\uparrow}(E_F) + D^{\downarrow}(E_F)} \tag{27}$$

where $D^{\uparrow}(E_F)$ is the density of states for spin-up electrons at energy $E$ and $D^{\downarrow}(E_F)$ is the density of states for spin-down electrons at energy $E_F$. The fully spin-up polarized systems would have $P = 1$ (*e.g.*, half-metal with only spin-up states at $E_F$), and the fully spin-down polarized systems would have $P = -1$, and if $P = 0$, then the system would not have spin polarization (equal DOS for both spins). Both total density of states (TDOS) and projected density of states (PDOS) were calculated based on spin-polarized crystal structure optimization. The states near the Fermi level ($E_F$) are critical in determining the electronic and magnetic properties. Generally, spin moments appear due to unequal occupancy of spin-up and spin-down bands and can be confirmed from the spin-polarized DOS deduced from the band structure calculations.[55]

The spin-polarized total density of states (TDOSs) and projected density of states (PDOS) of occupied d-orbitals of equiatomic HEB-1 over the energy range of −15 eV to +25 eV with the Fermi level ($E_F$) set to 0 eV are presented in Fig. 7(d), and for the rest of the compositions, are presented in the S7, SI. Spin down has been shown by inverting the *y*-axis with the same energy scale for the spin up contribution along the *x*-axis. Conductivity depends mainly on the electronic states near the Fermi surface. The non-zero d-orbital DOS at the Fermi level "$D(E_F)$" implies that the HEBs are intrinsically metallic, which has been indicated, due to orbital hybridization because of the overlap of d-orbital bands.[55] The overlaps of these bands give evidence that HEBs are composed of strong bonding. Along with this, the PDOS allows us to identify predominant states in conduction and valence bands near the Fermi level.[56] For almost all of the studied HEBs, it was observed that the PDOS was asymmetric with respect to the energy axis for all the metal atoms. This asymmetric distribution of spin-up and spin-down electrons in occupied and unoccupied states shows a hallmark of spin-polarization and near magnetism of the HEBs. Among all the compositions studied, HEB-1 ($Ti_{0.25}Zr_{0.25}Hf_{0.25}V_{0.25}B_2$), HEB-10 ($Ti_{0.08}Zr_{0.33}Hf_{0.33}V_{0.25}B_2$), HEB-11 ($Ti_{0.08}Zr_{0.25}Hf_{0.33}V_{0.33}B_2$), HEB-16 ($Ti_{0.33}Zr_{0.25}Hf_{0.17}V_{0.25}B_2$), and HEB-17 ($Ti_{0.17}Zr_{0.25}Hf_{0.25}V_{0.33}B_2$) showed the largest spin splitting, especially in the Ti-d and V-d states, suggesting magnetic moments localized on these atoms (Fig. 7(d) and S7, SI). The DOS of each HEB reflects how the variation in composition influences the position, intensity, and symmetry of the d-orbital contributions to DOS. Across all cases, the TDOS is predominantly governed by the d-orbitals of transition metals, particularly in the energy range from −10 eV to +15 eV. In some of the HEB configurations, clear spin polarization was observed, which indicates that these HEBs exhibit some degree of magnetism depending on the metal distribution.

Spin asymmetry is observed to be particularly pronounced in compositions having higher V and Ti concentrations. Titanium showed more pronounced peaks in the conduction band, particularly in the spin-up channel just above the Fermi level (0 to +5 eV). This behavior was noticeable in Ti-rich configurations such as HEB-1, HEB-16, and HEB-17, where 3d of Ti states dominates the low-energy conduction states, indicating its role in modulating electrical conductivity rather than contributing to deep valence band states; however, the spin asymmetry was less pronounced than that in the V-d contribution. The maximum contribution (5 and 7 electrons per eV near the Fermi level) in spin up for the valence band by the V-d orbital was observed for HEB-8 ($Ti_{0.08}Zr_{0.25}Hf_{0.42}V_{0.25}B_2$) and HEB-9 ($Ti_{0.08}Zr_{0.25}Hf_{0.25}V_{0.42}B_2$). Maximum contribution in spin down (up to 10 electrons per eV near the Fermi level) for the conduction band by the V-d orbital was observed for HEB-16 ($Ti_{0.33}Zr_{0.25}Hf_{0.17}V_{0.25}B_2$), HEB-1 ($Ti_{0.25}Zr_{0.25}Hf_{0.25}V_{0.25}B_2$), and HEB-17 ($Ti_{0.17}Zr_{0.25}Hf_{0.25}V_{0.33}B_2$) (Fig. 7(d) and S7, SI). However, the spin asymmetry is more pronounced than that in Ti-rich compositions, suggesting that V contributes to magnetism rather than being dominated by metallic conductivity. Zr-d and Hf-d in HEB systems exhibit broader and more localized d-states extending from −4 eV to +4 eV. These 4d and 5d elements contribute significantly to both the valence and conduction bands, with a relatively spin symmetric DOS. Because of their more itinerant nature, d-orbitals of Zr and Hf are primarily responsible for maintaining the metallic framework and minimizing exchange splitting (diminishing magnetism). In keeping with their function in ultra-high temperature ceramics, these components add structural rigidity and electron delocalization.[57]

Overall, most of the compositions displayed an asymmetric conduction band, with large spin-down contributions, particularly from Ti and V. Titanium contributed to compositions that lead to strong exchange splitting and enhanced magnetism due to localized d-states in the valence band. Vanadium was observed to contribute significantly near the Fermi level in both valence and conduction bands, favoring high electrical conductivity. Equiatomic $Ti_{0.25}Zr_{0.25}Hf_{0.25}V_{0.25}B$ (HEB-1) displayed a near symmetric spin, suitable for stable metallic applications without magnetic interference. Most of the non-equiatomic HEBs show good electrical conductivity and potential towards spintronic applications due to spin imbalance.

The total magnetic moment (Bohr magneton per formula unit, $\mu_B$ per f.u.) of the HEBs studied in the present work is reported in Table 4. The total magnetic moments of the HEBs ranged from 0.007 to $0.037\mu_B$ per f.u., indicating that the studied HEBs displayed a near non-magnetic nature or were weakly magnetic in their ground states. The small values of $\mu_B$ per f.u. suggest that the d-electrons of the transition metals, although capable of magnetic polarization individually, tend to become delocalized in the metallic and complex environment of the high-entropy solid solution. From the partial to total DOS, the valence band mostly consisted of s-orbitals. Generally, these lowest valence bands are separated from other valence bands by energy gaps for both majority (spin-up) and minority (spin-down) spin bands and are not affected by the exchange interaction.

Since the studied HEBs did not show any band gaps (Fig. 7(d) and S7, SI), it can be said that the s-orbitals do not influence the band gap and magnetic moment. The dispersed bands, which mainly consist of d-electrons, are due to the strong hybridization of orbitals, including p-electronic states. HEB-7 ($Ti_{0.42}Zr_{0.17}Hf_{0.17}V_{0.25}B_2$) showed the highest magnetic moment ($0.037\mu_B$ per f.u.) among all compositions. It may be due to a local imbalance in the electronic environment or increased contribution from the Ti and V atoms, which are known to exhibit weak magnetic behavior in some combinations. On the other hand, HEB-18 ($Ti_{0.33}Zr_{0.17}Hf_{0.25}V_{0.25}B_2$) showed the lowest moment of $0.007\mu_B$ per f.u., suggesting near-perfect cancellation of spin polarization. As can be seen from the S7, SI, the primary contribution to the total magnetic moment arises from spin polarization of d states. Hybridization of d states of the transition metals suggests the presence of metallic bonds. $D_{Ti}(E_F)$ and $D_V(E_F)$ are the highest among all PDOS at the Fermi level at all HEBs compositions, followed by $D_{Hf}(E_F)$ and $D_{Zr}(E_F)$, leading to magnetic instability. The spin-polarized PDOS of Ti and V have two separate peaks: one above the Fermi level and one below the Fermi level. These two peaks hybridize Hf and Zr peaks, respectively, resulting in magnetic splitting. Also, $D_{Hf}(E_F) \approx D_{Zr}(E_F)$, showing the very least DOS near the Fermi level, contributes to enhancing nonmagnetic characteristics.

### 3.6. Comparison of pure metal borides and high entropy diborides (HEBs)

To understand the superior properties of HEBs against the pure metal diborides, the properties such as elastic modulus, hardness, and melting point of the 18 HEB compositions are compared with the constituent metal diborides in Fig. 8.

Table 4 Magnetic moments of Ti, Zr, Hf and V based HEBs

| Nomenclature | HEB | Average spin up | Average spin down | Magnetic moment |
|---|---|---|---|---|
| HEB-1 | $Ti_{0.25}Zr_{0.25}Hf_{0.25}V_{0.25}B_2$ | 0.46 | 0.44 | 0.023 |
| HEB-2 | $Ti_{0.42}Zr_{0.25}Hf_{0.08}V_{0.25}B_2$ | 0.47 | 0.46 | 0.015 |
| HEB-3 | $Ti_{0.42}Zr_{0.25}Hf_{0.17}V_{0.17}B_2$ | 0.48 | 0.47 | 0.015 |
| HEB-4 | $Ti_{0.42}Zr_{0.17}Hf_{0.25}V_{0.17}B_2$ | 0.49 | 0.47 | 0.022 |
| HEB-5 | $Ti_{0.42}Zr_{0.08}Hf_{0.25}V_{0.25}B_2$ | 0.48 | 0.45 | 0.023 |
| HEB-6 | $Ti_{0.42}Zr_{0.25}Hf_{0.25}V_{0.08}B_2$ | 0.51 | 0.49 | 0.021 |
| HEB-7 | $Ti_{0.42}Zr_{0.17}Hf_{0.17}V_{0.25}B_2$ | 0.50 | 0.46 | 0.037 |
| HEB-8 | $Ti_{0.08}Zr_{0.25}Hf_{0.42}V_{0.25}B_2$ | 0.50 | 0.48 | 0.021 |
| HEB-9 | $Ti_{0.08}Zr_{0.25}Hf_{0.25}V_{0.42}B_2$ | 0.51 | 0.48 | 0.029 |
| HEB-10 | $Ti_{0.08}Zr_{0.33}Hf_{0.33}V_{0.25}B_2$ | 0.50 | 0.47 | 0.029 |
| HEB-11 | $Ti_{0.08}Zr_{0.25}Hf_{0.33}V_{0.33}B_2$ | 0.50 | 0.48 | 0.021 |
| HEB-12 | $Ti_{0.08}Zr_{0.33}Hf_{0.25}V_{0.33}B_2$ | 0.50 | 0.47 | 0.029 |
| HEB-13 | $Ti_{0.17}Zr_{0.25}Hf_{0.33}V_{0.25}B_2$ | 0.49 | 0.47 | 0.022 |
| HEB-14 | $Ti_{0.17}Zr_{0.25}Hf_{0.25}V_{0.33}B_2$ | 0.48 | 0.45 | 0.023 |
| HEB-15 | $Ti_{0.17}Zr_{0.33}Hf_{0.25}V_{0.25}B_2$ | 0.48 | 0.47 | 0.015 |
| HEB-16 | $Ti_{0.33}Zr_{0.25}Hf_{0.17}V_{0.25}B_2$ | 0.49 | 0.47 | 0.022 |
| HEB-17 | $Ti_{0.33}Zr_{0.25}Hf_{0.25}V_{0.17}B_2$ | 0.49 | 0.47 | 0.022 |
| HEB-18 | $Ti_{0.33}Zr_{0.17}Hf_{0.25}V_{0.25}B_2$ | 0.48 | 0.47 | 0.007 |

Fig. 8(a) shows that, except for HEB-1, HEB-9, and HEB-11, all the other 15 HEB compositions showed higher elastic moduli compared to $ZrB_2$, $VB_2$, and $TiB_2$. However, the elastic moduli of all 18 HEB compositions were observed to be less than that of $HfB_2$. Fig. 8(b) highlights that, except for HEB-8, HEB-9, HEB-11, and HEB-14, all the other 14 HEB compositions showed higher hardness compared to $ZrB_2$, $VB_2$, and $TiB_2$ but less than $HfB_2$. Furthermore, HEB-4, HEB-5, HEB-6, HEB-7, HEB-13, HEB-17, and HEB-18 showed higher melting points compared to the constituent metal diborides $ZrB_2$, $VB_2$, $HfB_2$, and $TiB_2$. Among the remaining HEBs, except for HEB-10, the other HEBs showed higher melting points than at least two pure metal diborides. This comparison confirms that the HEBs, having various concentrations of constituent metal diborides, have the potential to exhibit exceptionally enhanced mechanical and thermal stability compared to the pure metal diborides.

## 4. Conclusions

The present study introduces new types of high entropy diboride based ceramic materials comprised of transition metal diborides $TiB_2$, $HfB_2$, $ZrB_2$, and $VB_2$. There is only one literature study available for this combination, which reported the mechanical properties of equiatomic $(TiHfZrV)B_2$. The present study tried to assess the enhancement in the structural, mechanical, and thermal properties of this HEB combination by tuning the atomic fractions of Ti, Hf, Zr, and V. The phase and structural stability of the HEBs was confirmed using the thermodynamic parameters such as $\Delta H_{mix}$, $\Delta G_{mix}$, and $\Omega$ and the band-filling theory analysis. The findings conclusively show that compositional complexity governs the mechanical, thermodynamic, magnetic, and electronic behavior of the HEBs. Most of the HEB compositions ($Ti_{0.42}Zr_{0.25}Hf_{0.08}V_{0.25}B_2$, $Ti_{0.08}Zr_{0.25}Hf_{0.25}V_{0.42}B_2$, $Ti_{0.08}Zr_{0.25}Hf_{0.33}V_{0.33}B_2$, and $Ti_{0.33}Zr_{0.25}Hf_{0.25}V_{0.17}B_2$) met the criteria for single phase solid-solution formation as confirmed

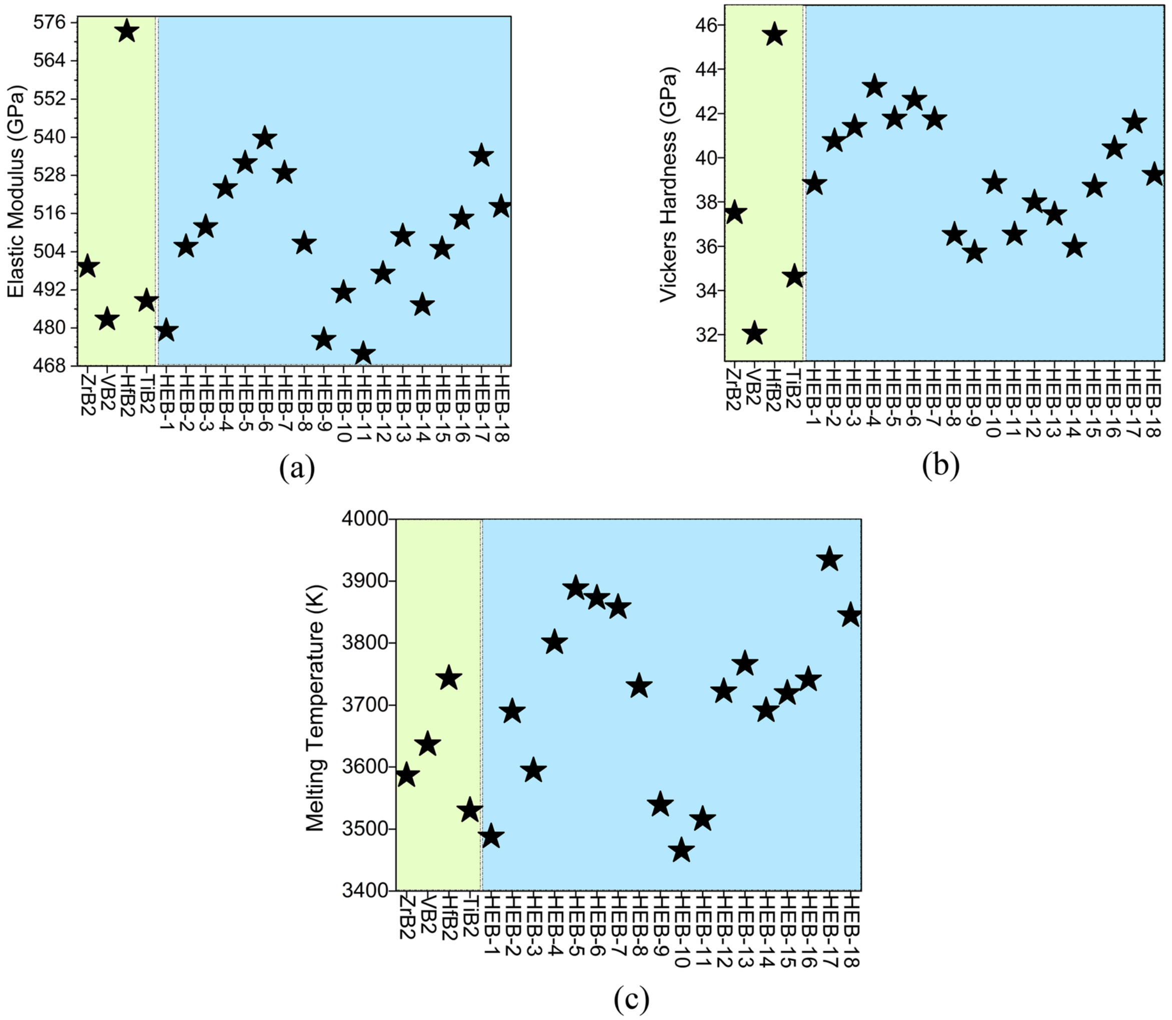

(a) (b) (c)

Fig. 8 Comparison of properties of Ti, Zr, Hf and V based HEBs with pure metal diborides: (a) elastic modulus, (b) hardness, and (c) melting temperature.

by thermodynamic parameters. According to the universal anisotropy index, which takes the differences in lattice symmetry and bonding uniformity into account, HEB-10 ($Ti_{0.08}Zr_{0.33}Hf_{0.33}V_{0.25}B_2$) showed the highest anisotropy, while HEB-4 ($Ti_{0.42}Zr_{0.17}Hf_{0.25}V_{0.17}B_2$) was nearly isotropic. With respect to mechanical stability, HEB-4 ($Ti_{0.42}Zr_{0.17}Hf_{0.25}V_{0.17}B_2$) having the highest Ti and Hf concentrations showed the highest hardness, while HEB-9 ($Ti_{0.08}Zr_{0.25}Hf_{0.25}V_{0.42}B_2$) and HEB-14 ($Ti_{0.17}Zr_{0.25}Hf_{0.25}V_{0.33}B_2$) having low concentrations of Ti and high concentration of V showed the lowest hardness. HEB-4 ($Ti_{0.42}Zr_{0.17}Hf_{0.25}V_{0.17}B_2$) appears to be the most brittle and isotropic, whereas HEB-9 ($Ti_{0.08}Zr_{0.25}Hf_{0.25}V_{0.42}B_2$) exhibited the highest ductility. With the highest Young's, shear, and bulk moduli, HEB-6 ($Ti_{0.42}Zr_{0.25}Hf_{0.25}V_{0.08}B_2$) having the highest Ti concentration and the lowest V concentration demonstrated remarkable elastic rigidity and superior resistance to both shape and volume deformation. The lowest Young's, shear, and bulk moduli of HEB-9 ($Ti_{0.08}Zr_{0.25}Hf_{0.25}V_{0.42}B_2$) and HEB-10 ($Ti_{0.08}Zr_{0.33}Hf_{0.33}V_{0.25}B_2$) suggest that low Ti concentrations and high V concentrations would make the HEBs compliant under mechanical loading and less rigid. The hardness of the studied HEBs ranged between 35.72 and 43.22 GPa, indicating their super-hardness properties. It is noteworthy that the Ti rich HEB-4 ($Ti_{0.42}Zr_{0.17}Hf_{0.25}V_{0.17}B_2$), HEB-6 ($Ti_{0.42}Zr_{0.25}Hf_{0.25}V_{0.08}B_2$), HEB-7 ($Ti_{0.42}Zr_{0.17}Hf_{0.17}V_{0.25}B_2$) and HEB-17 ($Ti_{0.33}Zr_{0.25}Hf_{0.25}V_{0.17}B_2$) displayed the potential to be superhard materials as their hardness was greater than 40 GPa, indicating their strong covalent bonding nature. Because of its low brittleness index and $H_V/E$ ratio, the Hf rich HEB-8 ($Ti_{0.08}Zr_{0.25}Hf_{0.42}V_{0.25}B_2$) having low Ti concentration showed the highest density, volume, and fracture toughness. HEB-8 displayed low wear resistance but excellent crack resistance. While magnetic variations (*e.g.*, high in HEB-7 ($Ti_{0.42}Zr_{0.17}Hf_{0.17}V_{0.25}B_2$)) result from variations in electronic hybridization and bonding type, the high Debye temperature and sound velocity in HEB-5 indicate strong atomic bonding and thermal stability. All non-equiatomic HEBs showed higher melting points than the equiatomic HEB-1. $Ti_{0.33}Zr_{0.25}Hf_{0.25}V_{0.17}B_2$ exhibited the highest melting point of 3934 K.

The complex composition of the investigated HEBs results in unique property–application relationships. Cutting tools and protective coatings may benefit from HEB-4 ($Ti_{0.42}Zr_{0.17}Hf_{0.25}V_{0.17}B_2$) due to its exceptional hardness and wear resistance.

For load-bearing structural elements, HEB-6 ($Ti_{0.42}Zr_{0.25}Hf_{0.25}V_{0.08}B_2$) may provide superior stiffness due to its highest elastic moduli. Strong crack resistance appropriate for armor and impact-resistant applications was displayed by HEB-8 ($Ti_{0.08}Zr_{0.25}Hf_{0.42}V_{0.25}B_2$) due to its high density and fracture toughness. HEB-9 ($Ti_{0.08}Zr_{0.25}Hf_{0.25}V_{0.42}B_2$) is suitable for flexible or heat shock-resistant structural coatings because it has the highest Poisson's ratio and ductility. HEB-5 ($Ti_{0.42}Zr_{0.08}Hf_{0.25}V_{0.25}B_2$) has outstanding thermal stability for high-temperature structural applications and aerospace applications due to its high Debye temperature and sound velocity. While HEB-17 ($Ti_{0.33}Zr_{0.25}Hf_{0.25}V_{0.17}B_2$) has the highest melting point and may be best suited for ultra-high-temperature applications like turbine blades and refractory coatings, HEB-7 ($Ti_{0.42}Zr_{0.17}Hf_{0.17}V_{0.25}B_2$), which exhibits the highest magnetic moment, may be a promising candidate for magnetic and spintronic devices. Overall, this study proves the importance of evaluating structure–property relationships to identify optimum HEC composition for a target application and also to identify non-equiatomic HEB compositions with superior properties compared to the usually explored equiatomic HEBs.

## Author contributions

Conceptualization: Yamini Sudha Sistla; methodology: Nabila Tabassum, Yamini Sudha Sistla; formal analysis and investigation: Nabila Tabassum; writing – original draft preparation: Nabila Tabassum; writing – review and editing: Yamini Sudha Sistla, supervision: Yamini Sudha Sistla.

## Conflicts of interest

There are no conflicts to declare.

## Data availability

No new data were generated or analysed as part of this work. Supporting data have been provided as part of the supplementary information (SI). Supplementary information is available. See DOI: https://doi.org/10.1039/d6ma00075d.

## Acknowledgements

The authors would like to acknowledge the SNU-Dassault Centre of Excellence (SDC) for providing the BIOVIA Material Studio software and Pipeline Pilot. The authors would also like to acknowledge Dr Ritwik Kavathekar, Dassault Systèmes, for providing technical guidance.

## References

1 A. Salian, P. Sengupta, I. Vishalakshi Aswath, A. Gowda and S. Mandal, A review on high entropy silicides and silicates: Fundamental aspects, synthesis, properties, *Int. J. Appl. Ceram. Technol.*, 2023, **20**, 2635–2660, DOI: 10.1111/ijac.14422.

2 L. Zeng, Z. Wang, J. Song, G. Lin, R. Guo, S. C. Luo, S. Guo, K. Li, P. Yu, C. Zhang, M. W. Guo, J. Ma, Y. Hou and H. Luo, Discovery of the high-entropy carbide ceramic topological superconductor candidate ($Ti_{0.2}Zr_{0.2}Nb_{0.2}Hf_{0.2}Ta_{0.2}$)C, *Adv. Funct. Mater.*, 2023, **33**, 2301929–2301937, DOI: 10.1002/adfm.202301929.

3 D. Liu, A. Zhang, J. Jia, J. Meng and B. Su, Phase evolution and properties of (VNbTaMoW)C high entropy carbide prepared by reaction synthesis, *J. Eur. Ceram. Soc.*, 2020, **40**, 2746–2751, DOI: 10.1016/j.jeurceramsoc.2020.03.020.

4 S. Barbarossa, R. Orrù, V. Cannillo, A. Iacomini, S. Garroni, M. Murgia and G. Cao, Fabrication and characterization of quinary high entropy-ultra-high temperature diborides, *Ceramics*, 2021, **4**, 108–120, DOI: 10.3390/ceramics4020010.

5 Q. Guo, H. Hou, Y. Pan, X. Pei, Z. Song, P. K. Liaw and Y. Zhao, Hardening-softening of $Al_{0.3}$CoCrFeNi high-entropy alloy under nanoindentation, *Mater. Des.*, 2023, **231**, 112050–112065, DOI: 10.1016/j.matdes.2023.112050.

6 L. Feng, W. G. Fahrenholtz and D. W. Brenner, High-entropy ultra-high-temperature borides and carbides: a new class of materials for extreme environments, *Annu. Rev. Mater. Res.*, 2021, **51**, 165–185, DOI: 10.1146/annurev-matsci-080819-121217.

7 A. C. Murchie, J. L. Watts, W. G. Fahrenholtz and G. E. Hilmas, Room-temperature mechanical properties of a high-entropy diboride, *Int. J. Appl. Ceram. Technol.*, 2022, **19**, 2293–2300, DOI: 10.1111/ijac.14026.

8 J. Liu, Q. Q. Yang, J. Zou, W. M. Wang, X. G. Wang and Z. Y. Fu, Strong high-entropy diboride ceramics with oxide impurities at 1800 °C, *Sci. China Mater.*, 2023, **66**, 2061–2207, DOI: 10.1007/s40843-022-2287-7.

9 Q. Li, C. Jiang and Y. Du, Molecular dynamics study on dynamic mechanical behaviour of FeCoCrCuNi high entropy alloy, *Mater. Technol.*, 2023, **38**, 1–11, DOI: 10.1080/10667857.2023.2200660.

10 F. Wang, F. Monteverde and B. Cui, Will high-entropy carbides and borides be enabling materials for extreme environments?, *Int. J. Extreme Manuf.*, 2023, **5**, 1–12, DOI: 10.1088/2631-7990/acbd6e.

11 L. Qiao, Y. Liu, Y. Gao, J. Bi, Y. Li and C. Liu, *et al.*, First-principles prediction, fabrication and characterization of ($Hf_{0.2}Nb_{0.2}Ta_{0.2}Ti_{0.2}Zr_{0.2}$)$B_2$ high-entropy borides, *Ceram. Int.*, 2022, **48**, 17234–17245, DOI: 10.1016/j.ceramint.2022.02.281.

12 B. Storr, L. Moore, K. Chakrabarty, Z. Mohammed, V. Rangari and C. C. Chen, *et al.*, Properties of high entropy borides synthesized *via* microwave-induced plasma, *APL Mater.*, 2022, **10**, 1–10, DOI: 10.1063/5.0098276.

13 J. Gild, Y. Zhang, T. Harrington, S. Jiang, T. Hu, M. C. Quinn, W. M. Mellor, N. Zhou, K. Vecchio and J. Luo, High-entropy metal diborides: a new class of high-entropy materials and a new type of ultrahigh temperature ceramics, *Sci. Rep.*, 2016, **6**, 1–10, DOI: 10.1038/srep37946.

14 A. C. Feltrin, D. Hedman and F. Akhtar, Transformation of metastable dual-phase ($Ti_{0.25}V_{0.25}Zr_{0.25}Hf_{0.25}$)$B_2$ to stable

high-entropy single-phase boride by thermal annealing, *Appl. Phys. Lett.*, 2021, **119**, 161905, DOI: 10.1063/5.0066698.

15 S. Y. Liu, S. Zhang, S. Liu, D. J. Li, Y. Li and S. Wang, Phase stability, mechanical properties and melting points of high-entropy quaternary metal carbides from first-principles, *J. Eur. Ceram. Soc.*, 2021, **41**, 6267–6274, DOI: 10.1016/j.jeurceramsoc.2021.05.022.

16 R. Z. Zhang and M. J. Reece, Review of high entropy ceramics: Design, synthesis, structure and properties, *J. Mater. Chem. A*, 2019, **7**, 22148–22162, DOI: 10.1039/c9ta05698j.

17 T. Wen, B. Ye, M. C. Nguyen, M. Ma and Y. Chu, Thermophysical and mechanical properties of novel high-entropy metal nitride-carbides, *J. Am. Ceram. Soc.*, 2020, **103**, 6475–6489, DOI: 10.1111/jace.17333.

18 A. A. Deshmukh and R. Ranganathan, Recent advances in modelling structure-property correlations in high-entropy alloys, *J. Mater. Sci. Technol.*, 2025, **204**, 127–151, DOI: 10.1016/j.jmst.2024.03.027.

19 A. Roy and G. Balasubramanian, Predictive descriptors in machine learning and data-enabled explorations of high-entropy alloys, *Comput. Mater. Sci.*, 2021, **193**, 110381, DOI: 10.1016/j.commatsci.2021.110381.

20 N. Y. Yurchenko, N. D. Stepanov, D. G. Shaysultanov, M. A. Tikhonovsky and G. A. Salishchev, Effect of Al content on structure and mechanical properties of the $Al_xCrNbTiVZr$ ($x = 0$; 0.25; 0.5; 1) high-entropy alloys, *Mater. Charact.*, 2016, **121**, 125–134, DOI: 10.1016/j.matchar.2016.09.039.

21 N. Tabassum and Y. S. Sistla, Thermal stability assessment of mixed phase AlCoCrFeNi high entropy alloy: In silico studies, *Phys. B*, 2025, **712**, 417319, DOI: 10.1016/j.physb.2025.417319.

22 N. Tabassum, Y. S. Sistla, R. G. Burela and A. Gupta, Structural, electronic, mechanical and thermal properties of $Al_xCoCrFeNi$ ($0 \leq x \leq 2$) high entropy alloy using density functional theory, *Met. Mater. Int.*, 2024, **30**, 3349–3369, DOI: 10.1007/s12540-024-01709-6.

23 F. Liang, J. Du, G. Su, C. Xu, C. Zhang and X. Kong, Phase stability and mechanical properties analysis of $AlCo_xCrFeNi$ HEAs based on first principles, *Metals*, 2022, **12**, 1–9, DOI: 10.3390/met12111860.

24 J. Gao, Q. J. Liu and B. Tang, Elastic stability criteria of seven crystal systems and their application under pressure: Taking carbon as an example, *J. Appl. Phys.*, 2023, **133**, 1–9, DOI: 10.1063/5.0139232.

25 H. Zhang, X. Sun, S. Lu, Z. Dong, X. Ding, Y. Wang and L. Vitos, Elastic properties of $Al_xCrMnFeCoNi$ ($0 \leq x \leq 5$) high-entropy alloys from *ab initio* theory, *Acta Mater.*, 2018, **155**, 12–22, DOI: 10.1016/j.actamat.2018.05.050.

26 Y. Tian, B. Xu and Z. Zhao, Microscopic theory of hardness and design of novel superhard crystals, *Int. J. Refract. Met. Hard Mater.*, 2012, **33**, 93–106, DOI: 10.1016/j.ijrmhm.2012.02.021.

27 H. Niu, S. Niu and A. R. Oganov, Simple and accurate model of fracture toughness of solids, *J. Appl. Phys.*, 2019, **125**, 065105, DOI: 10.1063/1.5066311.

28 H. Liang, W. Sun, X. Li, H. Chen, S. Guan and P. Liu, *et al.*, Study of the compression behavior and elastic properties of $HfB_2$ ceramics using experimental method and first-principles calculations, *J. Alloys Compd.*, 2019, **808**, 151764, DOI: 10.1016/j.jallcom.2019.151764.

29 P. Sharma and G. Balasubramanian, Electronic and lattice distortions induce elastic softening in refractory multicomponent borides, *Chem. Mater.*, 2023, **35**, 1–10, DOI: 10.1021/acs.chemmater.3c01086.

30 P. J. Robinson, G. Liu, S. Ciborowski, M. C. Martinez, J. R. Chamorro and X. Zhang, *et al.*, Mystery of Three Borides: Differential metal–boron bonding governing superhard structures, *Chem. Mater.*, 2017, **29**, 9892–9896, DOI: 10.1021/acs.chemmater.7b04378.

31 G. Will, Electron deformation density in titanium diboride chemical bonding in $TiB_2$, *J. Solid State Chem.*, 2004, **177**, 628–631, DOI: 10.1016/j.jssc.2003.04.008.

32 J. Gild, M. Samiee, J. L. Braun, T. Harrington, H. Vega, P. E. Hopkins, K. Vecchio and J. Luo, High-entropy fluorite oxides, *J. Eur. Ceram. Soc.*, 2018, **38**, 3578–3584, DOI: 10.1016/j.jeurceramsoc.2018.04.010.

33 R. G. Munro, Material properties of titanium diboride, *J. Res. Natl. Inst. Stand. Technol.*, 2000, **105**, 1–12.

34 R. Gaillac, P. Pullumbi and F. X. Coudert, ELATE: An open-source online application for analysis and visualization of elastic tensors, *J. Phys.: Condens. Matter*, 2016, **28**, 1–10, DOI: 10.1088/0953-8984/28/27/275201.

35 Y. Yang, H. Lu, C. Yu and J. M. Chen, First-principles calculations of mechanical properties of TiC and TiN, *J. Alloys Compd.*, 2009, **485**, 542–547, DOI: 10.1016/j.jallcom.2009.06.023.

36 J. Song, G. Chen, H. Xiang, F. Dai, S. Dong, W. Han, X. Zhang and Y. Zhou, Regulating the formation ability and mechanical properties of high-entropy transition metal carbides by carbon stoichiometry, *J. Mater. Sci. Technol.*, 2022, **121**, 181–189, DOI: 10.1016/j.jmst.2021.12.063.

37 S. Mousavinasab and C. Blais, Study of the effect of microstructure heterogeneity on fatigue crack propagation of low-alloyed PM steels, *Mater. Sci. Eng., A*, 2016, **667**, 444–453, DOI: 10.1016/j.msea.2016.05.025.

38 G. Cheng, J. X. Liu, Y. Qin, Y. Wu and G. J. Zhang, Thermal conductivity of equiatomic high-entropy diboride ceramics with 5–9 cations, *Int. J. Appl. Ceram. Technol.*, 2023, **20**, 2708–2716.

39 W. D. Callister Jr and D. G. Rethwisch, *Materials Science and Engineering: An Introduction*, 10th edn, 2018, pp. 1–975.

40 S. J. McMaster, S. Kosarieh, T. W. Liskiewicz, A. Neville and B. D. Beake, Utilising H/E to predict fretting wear performance of DLC coating systems, *Tribol. Int.*, 2023, **185**, 108524–108534, DOI: 10.1016/j.triboint.2023.108524.

41 H. Xiang, Y. Xing, F. Z. Dai, H. Wang, L. Su, L. Miao, G. Zhang, Y. Wang, X. Qi, L. Yao, H. Wang, B. Zhao, J. Li and Y. Zhou, High-entropy ceramics: Present status, challenges, and a look forward, *J. Adv. Ceram.*, 2021, **10**, 385–441, DOI: 10.1007/s40145-021-0477-y.

42 Y. Wang, J. Zhang, T. Wu and G. Huang, Full-scale insight into high-entropy ceramics from basic concepts, synthesis

technologies, structural characteristics, and properties to application prospects, *J. Mater. Res. Technol.*, 2024, **33**, 398–430, DOI: 10.1016/j.jmrt.2024.09.063.

43 S. I. Ranganathan and M. Ostoja-Starzewski, Universal elastic anisotropy index, *Phys. Rev. Lett.*, 2008, **101**, 1–4, DOI: 10.1103/PhysRevLett.101.055504.

44 T. S. Duffy, Single-crystal elastic properties of minerals and related materials with cubic symmetry, *Am. Mineral.*, 2018, **103**, 977–988, DOI: 10.2138/am-2018-6285.

45 C. Kittel, *Solid State Physics*, John Wiley & Sons Inc., Hoboken, New Jersey, 8th edn, 2005.

46 A. Kirnbauer, C. Spadt, C. M. Koller, S. Kolozsvári and P. H. Mayrhofer, High-entropy oxide thin films based on Al–Cr–Nb–Ta–Ti, *Vacuum*, 2019, **168**, 108850, DOI: 10.1016/j.vacuum.2019.108850.

47 M. Sajidul Islam, R. Ahmed, M. Mahamudujjaman, R. S. Islam and S. H. Naqib, A comparative study of the structural, elastic, thermophysical, and optoelectronic properties of $CaZn_2X_2$ (X = N, P, As) semiconductors *via* ab-initio approach, *Results Phys.*, 2023, **44**, 1–18, DOI: 10.1016/j.rinp.2023.106214.

48 Z. Wang, G. Liu, W. Gao, Y. Yang, T. Zheng, Z. Q. Liu, P. Peifeng Li, M. Yan and Y. D. Fu, Mechanical behavior of high entropy ceramic $(TiZrHfVNb)C_5$ under extreme conditions: A first-principles density functional theory study, *Ceram. Int.*, 2024, **50**, 9820–9831, DOI: 10.1016/j.ceramint.2023.12.304.

49 I. Mayer, *Simple Theorems, Proofs, and Derivations in Quantum Chemistry*, Springer Science & Business Media, New York, 2003, pp. 1–337.

50 C. Jin, K. Xiong, L. Guo, Z. Sun, W. Li, S. Zhang, W. Li, S. Zhang, Y. Wang and Y. Ma, A DFT insight into the mechanical, electronic and thermodynamic properties of (TiZrHf)C medium-entropy carbide ceramic, *Results Phys.*, 2022, **35**, 1–10, DOI: 10.1016/j.rinp.2022.105341.

51 H. Liu, J. Zhu, Y. Liu and Z. Lai, First-principles study on the mechanical properties of vanadium carbides VC and $V_4C_3$, *Mater. Lett.*, 2008, **62**, 3084–3086, DOI: 10.1016/j.matlet.2008.01.136.

52 R. Trivedi, A. Banerjee and D. Bandyopadhyay, Study of electronic structure, stabilities and electron localization behavior of AgPbn (n = 1–14) nanoclusters: A first principal investigation, *Phys. E*, 2021, **131**, 114725, DOI: 10.1016/j.physe.2021.114725.

53 Y. Guo, X. Zhang, Z. Huang, J. Chen, Z. Luo, J. Zhang, J. Li, Z. Zhang, J. Zhao, X. Han and H. Wu, Quantum materials for spintronic applications, *npj Spintron.*, 2024, **2**, 1–11, DOI: 10.1038/s44306-024-00038-z.

54 S. Ram, S. Biswas and J. H. Fecht, Advanced ceramics and nanocomposites of half-metallic ferromagnetic $CrO_2$ for magnetic, GMR and optical sensors, *Funct. Nanostructures Process. Charact. Appl.*, 2007, pp. 1–64. , DOI: 10.1007/978-0-387-48805-9_1.

55 Y. P. Wang, G. Y. Gan, W. Wang, Y. Yang and B. Y. Tang, *Ab initio* prediction of mechanical and electronic properties of ultrahigh temperature high-entropy ceramics $(Hf_{0.2}Zr_{0.2}Ta_{0.2}M_{0.2}Ti_{0.2})B_2$ (M = Nb, Mo, Cr), *Phys. Status Solidi B*, 2018, **255**, 1–7, DOI: 10.1002/pssb.201800011.

56 S. Wang, T. Zhang, H. Hou and Y. Zhao, The magnetic, electronic, and thermodynamic properties of high entropy alloy CrMnFeCoNi: A first-principles study, *Phys. Status Solidi B*, 2018, **255**, 1–6, DOI: 10.1002/pssb.201800306.

57 B. R. Golla, A. Mukhopadhyay, B. Basu and S. K. Thimmappa, Review on ultra-high temperature boride ceramics, *Prog. Mater. Sci.*, 2020, **111**, 100651, DOI: 10.1016/j.pmatsci.2020.100651.